Chemical Geology 493 (2018) 37–57

Contents lists available at ScienceDirect

Chemical Geology

journal homepage: www.elsevier.com/locate/chemgeo

Hydrogeochemical fluxes and processes contributing to the formation of lithium-enriched brines in a hyper-arid continental basin

Lee Ann Munk[a,*], David F. Boutt[b], Scott A. Hynek[c,1], Brendan J. Moran[b]

[a] Department of Geological Sciences, 3101 Science Circle, University of Alaska-Anchorage, Anchorage, AK, USA
[b] Department of Geosciences, University of Massachusetts-Amherst, Amherst, MA, USA
[c] University of Utah, Department of Geology and Geophysics, Salt Lake City, UT, USA

ARTICLE INFO

Editor: K. Johannesson

Keywords:
Lithium
Brines
Salar de Atacama
Chile
Hydrogeochemistry
Solutes
Fluxes
Hyper-arid

ABSTRACT

The accumulation of solutes delivered via shallow groundwater and surface water in arid to hyper-arid closed basins, and the complex hydrogeochemical processes associated with their transport, are key to deciphering mechanisms responsible for the formation of brines and salts in these environments. A rigorous investigation of the hydrogeochemical fluxes and the formation of the Li-enriched brine in the hyper-arid basin of the Salar de Atacama, Chile is presented. Water fluxes within the Salar de Atacama basin range from 0.003 m^3/s to 1.50 m^3/s with a poor correlation between discharge and drainage basin area. The inflowing waters have major elemental and Li concentrations that are within the same order of magnitude over a period of several decades. The element fluxes indicate, for example, that 58% of the Li in the halite nucleus and brines is derived from the south and southeast parts of the basin. The average $\delta^{18}O_{vsmow}$ and δD_{vsmow} of inflow waters indicate that there are varied sources of recharge corresponding to the defined sub watershed regions. The average water flux-weighted $^{87}Sr/^{86}Sr$ of inflow waters allows further definition of where in the regional watershed the solutes are derived. The predicted water flux weighted $^{87}Sr/^{86}Sr$ of the brines (0.70813) compared to the measured average $^{87}Sr/^{86}Sr$ (0.70801), indicates that there may be unaccounted sources of water and solutes to the basin brines. Elemental accumulation time scales for the volume of halite and brine in the nucleus balance on time frames of 0.5 Ma (Mg), 1.0 Ma (Ca), 1.9 Ma (Li) and 2.2 Ma (K) as compared to 47 Ma (Na) and 53 Ma (Cl), further evidence that Na and Cl require additional sources not accounted for in the modern inflows to the topographic watershed. Dissolved noble gas concentrations of marginal and nucleus brines specify that the brines formed in an atmospheric equilibrated state and have since been isolated below the salt crust. A process-based model is presented to explain the extremely high concentrations of Li in brines which incorporates the δ^7Li isotope signatures of waters in the basin to further decipher, on a first order, the contributions of processes such as low temperature weathering and secondary phase formation.

1. Introduction

Elemental fluxes delivered via groundwater are the ultimate sources of solutes that are transported and accumulated as brine bodies in evaporite systems (Warren, 2016). In arid to hyper-arid climate conditions where the groundwater discharges near the land surface accompanied by basin subsidence and where conditions of chemical saturation persist, thick accumulations of evaporite salts and associated brines may form (Warren, 2016). These processes occur in both mature and immature salar depositional environments (Houston et al., 2011) and result in brines that contain varying amounts of the major cations and anions (Na, K, Mg, Ca, Cl, SO_4, HCO_3 and CO_3) which can form a range of ionic salts once they reach saturation, but may also be redissolved based on the amount of water influxing (Warren, 2010). Hydrothermal and/or geothermal influences on groundwater may also alter the composition of the inflowing waters to basins (Lowenstein and Risacher, 2009). The composition of the source rocks and the resulting brine composition dictate how the brine will evolve once it undergoes evaporation and mineral precipitation (Eugster, 1980). These brines can also contain appreciable concentrations of Li, B, Ba, Sr, Br, I, and F, and in the case where Li is concentrated on the order of 100 s of mg/L these deposits can be classified as having potential economic viability with respect to Li extraction. The most notable of these salars and brines is the Salar de Atacama, Chile and its associated Li-rich brine which

* Corresponding author.
E-mail address: lamunk@alaska.edu (L.A. Munk).
[1] Present affiliation: U.S. Geological Survey, Utah Water Science Center, Salt Lake City, Utah, USA.

https://doi.org/10.1016/j.chemgeo.2018.05.013
Received 19 February 2018; Received in revised form 6 May 2018; Accepted 8 May 2018
Available online 10 May 2018
0009-2541/

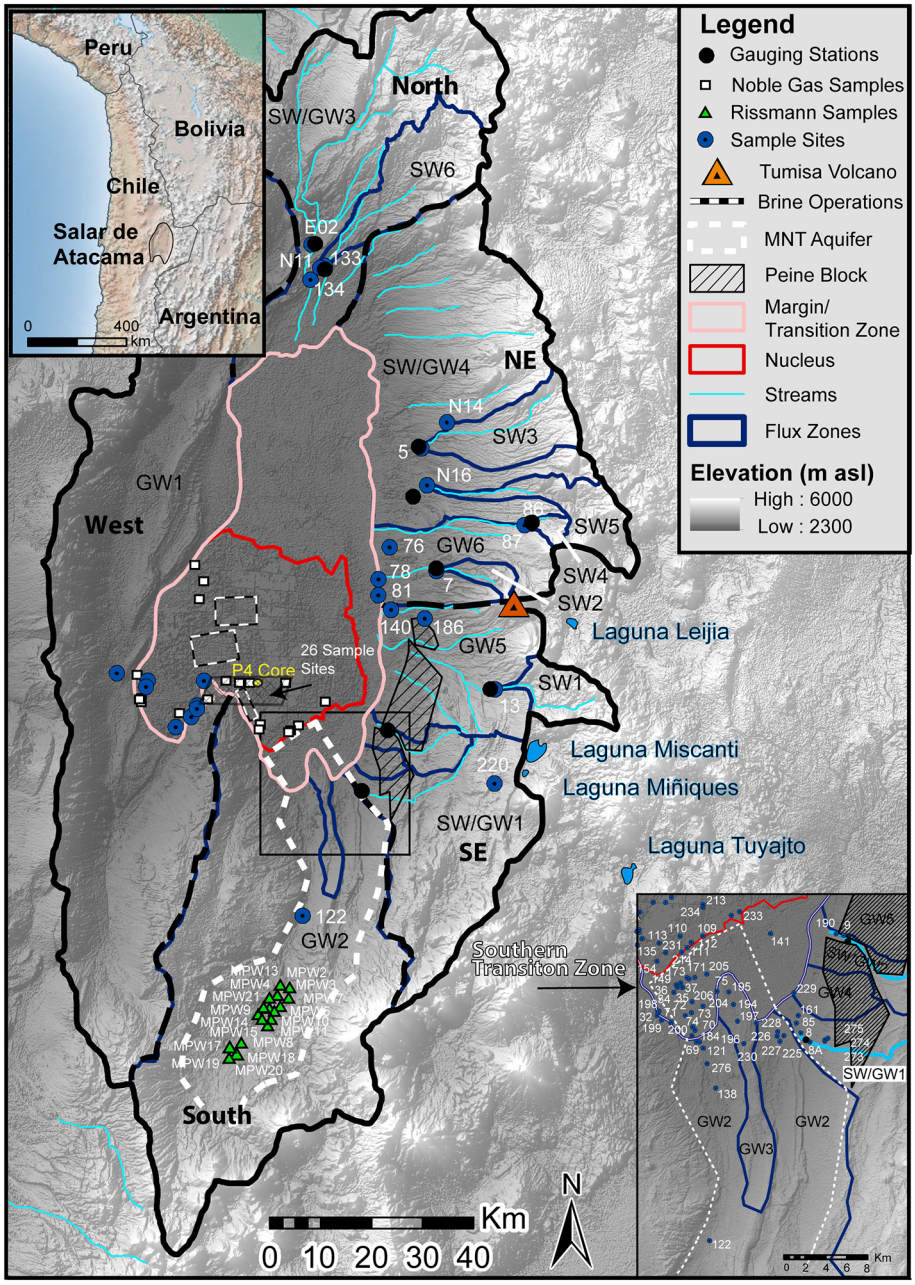

Fig. 1. Digital elevation map of the Salar de Atacama, Chile basin illustrating the topographic watershed, the five watershed regions defined in this study (west, north, northeast, southeast and south) and the surface and groundwater flux basins (ie. SW, GW) within each. The sample locations are also shown. The MNT aquifer, brine production facilities and other important features are highlighted.

contains on average 1400 mg/L Li (Munk et al., 2016a and refs. within).

The Salar de Atacama (SdA) is a giant active closed-basin on the western flank of the Central Andean Plateau (CAP) situated on the Tropic of Capricorn in the hyper-arid Atacama Desert (Fig. 1) where active evaporite deposition is occurring. The basin may have been hydrographically closed for the entire Cenozoic Era, since ~66 Ma, but began accumulating the massive halite nucleus ~6–10 Ma coincident with uplift of the CAP (Jordan et al., 2002a, 2002b, 2010). In addition to accumulating about 1800 km^3 of halite in the nucleus over this interval, a voluminous brine deposit has formed and is now hosted in halite aquifers and other geologic units including volcanic rocks within the nucleus of the salar. This brine contains some of the highest known concentrations of Li (up to 7000 mg/L reported historically) of any continental brine (Ide and Kunasz, 1989; Munk et al., 2016a).

The generation of the large evaporite deposit and the economic Li-rich brine in the SdA cannot be explained by the modern hydrology and climate. Recently, Corenthal et al. (2016) showed that in order to sustain halite accumulation in the basin from the late Miocene to the present it would require the long-term discharge to the basin to be on the order of 9–20 times more than the modern. These types of deposits are distinctive on a global scale, and understanding their origin is a key step in developing process-based models to explain them. There are a projected 16 Mt of Li reserves in the world and 7.5 Mt of lithium reserves in Chile most of which are in the SdA Li-brine deposit (USGS, 2018). Approximately 14,100 t (33%) out of the global total of 43,000 t (excluding U.S. production) of Li were produced from Chile in 2017 (USGS, 2018).

Continental brines have been most extensively investigated in the Central Andes of Bolivia and northern Chile as reported in Risacher et al. (2003) and Risacher and Fritz (2009) and references therein.

Hundreds of geochemical analyses for brines from this region are published by Moraga (1974), Rettig et al. (1980), Risacher and Fritz (1991), Risacher et al. (1999), and Risacher et al. (2003). The focus of this previous work was to examine the origin of the salts in the salars. Risacher and Fritz (2009) also provide a general classification for these brines (alkaline, sulfate-rich and calcium-rich), and noted that alkaline salars are absent in Chile due to the presence of high-sulfur volcanic rocks. The origin of solutes to salars in the Central Andes has been addressed by the major and trace element and isotopic investigations of Alpers and Whitmore (1990), Spiro and Chong (1996), Carmona et al. (2000), Boschetti et al. (2007), and Rissmann et al. (2015). Solute mass flux for surface drainages and a few groundwater drainages in the Salar de Atacama were estimated by Alonso and Risacher (1996). Rissmann et al. (2015) indicated that waters from higher elevation Andean salars are entrained in the regional groundwater of the southern aquifer system in the SdA basin, highlighting the importance of this process to the overall solute budget. However, none of these studies incorporate rigorous water flux weighted solute concentrations or a regional mass balance approach which is what makes our contribution unique and novel. We use the most robust data set from both surface and shallow groundwater solute concentrations in order to calculate the mass balance of Li and associated major ions and the geochemical behavior of these ions in this evaporative continental basin setting. We present the results of a six-year investigation (2011–2016) that includes multiple surface and groundwater sampling sites with seasonal geochemical data in order to document the modern geochemical fluxes to the basin and to constrain the mechanisms responsible for the formation of the world's most enriched Li brine.

This work has established a rigorous and robust basin-wide analysis of water and solute fluxes and identifies the hydrogeochemical processes responsible for the formation of the Li-enriched brine. The approach to this work is based on field observations, measurements and calculations of water flux and Li, Na, K, Ca, Mg, and Cl concentrations in dilute inflow waters from the south, southeast, northeast, north and west parts of the basin as well as basin brines in the halite nucleus, its margin, and the transition zone (Fig. 1). The assessment of solute fluxes further supported by $\delta^{18}O$, δD and $^{87}Sr/^{86}Sr$ signatures of the inflow waters and dissolved noble gas chemistry of brines is followed by an elemental mass balance approach to compare the total modern flux of solutes into the basin to the estimated masses of these elements stored in the halite nucleus (in brine and halite) of the salar. Deviations from the observed versus predicted/calculated geochemical signatures indicate that there are unidentified sources of water and/or solutes present in the brine and that subtleties in the geochemical behavior of major elements and Li must be considered. Finally, the primary geochemical and hydrogeologic processes that operate to concentrate the brine and Li to the highest observed concentrations of any Li-brine deposit are addressed.

2. Geologic setting and hydrogeology of the Salar de Atacama basin

The SdA coincides with a sharp bend in the modern Andean volcanic arc which retreats 60 km east from its regional north-south trend. The salar surface has an area of 3000 km^2, and a drainage basin flanked on all sides by substantial relief; the Andean volcanic arc dominates recharge to the salar. The salar surface is 2300 m above sea level, and is ~2000 m lower than the volcanic arc. Precipitation on the salar surface is rare but documented (Boutt et al., 2016), adjacent Andean highlands receive more precipitation, but are still arid to hyper-arid (Strecker et al., 2007). Evaporation at the elevation of the salar varies between 0 and 2.8 mm/d depending on the surface characteristics (Kampf et al., 2005); relative to estimated mean annual precipitation of 39 mm (0.1 mm/d). Water in the basin varies in Li concentration from near 0.05–5 mg/L for inflow waters, 5–100 mg/L Li in shallow groundwaters in the southern and eastern flanks of the basin and in excess of 5000 mg/L in brines (Munk et al., 2016a). Thus, the brines in the basin are up to five orders of magnitude more concentrated than near-surface water entering the basin.

The salar is divided into two distinct morphologic zones. In the north, the eastern slope of the basin is characterized by monoclinal folding blanketed by thick ignimbrite deposits and alluvial fans (e.g. Reutter et al., 2006; Jordan et al., 2010). To the south, the low permeability Peine block, bounded by the north-south trending Peine Fault System to the west and Quebrada de Nacimiento Fault to the east, separates the salar from the Andes (Ramirez and Gardeweg, 1982; Aron et al., 2008). Alluvial fans that occur around the salar are important for transporting fluid to the marginal zones (Mather and Hartley, 2005), but large aquifer systems are not well defined. The most notable aquifer due to its size is the Monturaqui-Negrillar (MNT) system in the south. Unwelded to moderately welded ignimbrites in the basin have high infiltration capacity and permeability, while the welded ignimbrites may act as confining units (Lameli, 2011; Houston, 2009). Recent and ongoing work on a set of sediment cores from the south part of the basin and the halite nucleus indicate a complex hydrostratigraphy of sand and gravel, ash and ignimbrite, and evaporites (Munk et al., 2014). The low permeability Peine block (Lameli, 2011) diverts groundwater flow to the north and south, while the zone of monoclinal folding is expected to be more conducive to regional groundwater flow based on laterally extensive strata dipping towards the salar (Jordan et al., 2002a, 2002b). The blind, high-angle, down-to-the-east north-south trending reverse Salar Fault System (SFS) which cuts across the salar accommodates over 1 km of offset of basin fill strata (Jordan et al., 2007; Lowenstein et al., 2003). Jordan et al. (2002b) suggest the SFS acts as a barrier to groundwater flow causing orogenic scale groundwater flow to discharge in the salar center, but this idea is yet untested. Regional groundwater flow from the Andean Cordillera downgradient to the Pampa del Tamarugal northwest of SdA has been suggested by Pérez-Fodich et al. (2014), in areas north of the SdA (Magaritz et al., 1990; Montgomery et al., 2003) and from the Altiplano-Puna plateau to the SdA (Jordan et al., 2002b). Evidence for modern recharge in the central high Andes is widespread (Magaritz et al., 1990; Aravena, 1995; Houston, 2007) although the rates and spatial extent are poorly constrained (Grosjean et al., 1995; Houston, 2009).

Our work has established that the modern (Boutt et al., under review) and paleo water (Corenthal et al., 2016) budget of the basin is considerably out of balance suggesting that either 1) water is being sourced from outside of the topographic divides and/or 2) being balanced by transient drawdown of the water table (i.e. storage). These questions of hydrologic balance are critical to determining the flux of Li and other solutes including Na, K, Ca, Mg and Cl in this system which accumulate to form the giant evaporite and brine deposit in the basin. Here we investigate a step further by 1) using mass balance of the major ions and Li to further develop the model of solute accumulation in the basin and 2) analyzing multiple geochemical and isotopic signatures to determine sources of water and solutes and to explain the formation of the brine deposit.

3. Methods and analysis

3.1. Water

Surface and shallow groundwater samples were collected over the period 2011–2016 and in most cases the sampling occurred on a seasonal basis from the same locations. However, not all of the same sites were visited during each sampling event therefore, our approach is to use representative elemental averages weighted by respective water fluxes for each watershed region contribution. Table 2 lists all of the sampling events and the minimum, maximum and averages for each event including the number of sites sampled for each watershed region. Sampling locations and ID's that are used in this study are shown in Fig. 1 and the sample dates and other relevant information are provided

Table 1
Five watershed zones for the SdA basin, contributing areas, and calculated water and elemental fluxes.

Watershed Zone	Water Flux (m^3/s)	Contributing Area (km^2)	Li (g/s)	Na (g/s)	K (g/s)	Mg (g/s)	Ca (g/s)	Cl (g/s)
MNT (GW2)	0.468	3,185	1.2	254.5	25.8	56.3	61.0	425.2
Tilocalar (GW3)	0.045	84	0.2	73.7	17.1	12.6	15.5	101.4
South Inflow	***0.513***	3,269	***1.5***	***328.2***	***42.8***	***68.9***	***76.5***	***526.6***
Rio Tulan (SW/GW1)	0.152	1,029	0.3	134.3	10.6	26.9	28.3	244.9
A well (GW4)	0.108	50	0.2	89.3	7.7	22.6	15.2	139.9
Rio Peine (SW/GW2)	0.221	130	0.1	105.0	6.0	31.4	57.5	182.8
Diffuse south Tumisa (GW5)	0.554	754	0.5	119.9	5.9	17.1	62.3	144.6
Rio Socaire (SW1)	0.17	169	0.0	17.5	2.6	8.6	9.5	18.5
Southeast Inflow	***1.205***	2,132	***1.1***	***466.0***	***32.7***	***106.6***	***172.9***	***730.7***
Rio Camar (SW2)	0.003	56	0.0	0.9	0.1	0.4	0.4	0.8
Diffuse north Tumisa gw (GW6)	0.225	474	0.3	97.9	7.8	39.7	54.3	94.9
Rio Honar (SW3)	0.061	298	0.0	2.1	0.3	0.7	0.9	2.9
Rio Talabre (SW4)	0.006	32	0.0	0.3	0.0	0.2	0.2	0.3
Aquas Blancas (SW5)	0.15	246	0.2	47.6	4.3	4.0	13.4	43.0
Diffuse north east gw (SW/GW4)	0.891	1,815	0.1	28.8	2.0	4.7	13.7	27.1
Northeast Inflow	***1.336***	2,921	***0.6***	***177.5***	***14.5***	***49.7***	***82.9***	***169.1***
Rio San Pedro (SW/GW3)	1.5	1,681	0.6	727.8	22.1	47.0	182.2	982.4
Rio Vilama (SW6)	0.218	420	0.6	88.7	8.0	12.7	24.3	139.8
North Inflow	***1.718***	2,101	***1.2***	***816.5***	***30.0***	***59.7***	***206.4***	***1122.2***
West (GW1)	0.033	4,261	0.0	3.1	0.0	0.0	0.1	4.2
West Inflow	***0.033***	4,261	***0.0***	***3.1***	***0.0***	***0.0***	***0.1***	***4.2***
Total	***4.81***	14,684	4.4	1791.3	120.2	284.9	538.8	2552.8

in Tables 2 and 3.

Water samples for dissolved major and minor elements, anions and stable isotopes of hydrogen and oxygen ($\delta^{18}O$ and δD) were collected at each location. At select sites samples for Sr and Li isotopes and dissolved noble gas analyses were also collected. Water samples were filtered through 0.45 μm filters using a plastic 60 mL syringe and were stored in clean HDPE bottles. Samples for elemental and Sr and Li isotope analyses were acidified with ultra-pure nitric acid. In-situ measurements of temperature, specific conductance, and pH were made at each sampling location at the time of sample collection.

The concentration of major ions and trace elements in the water samples were analyzed using inductively coupled plasma mass spectrometry with a reaction cell for major elements and Li (ICP RC-MS, Agilent 7500c) and ion chromatograph (Dionex ICS 5000 +) for Cl and SO_4 anions at the University of Alaska Anchorage. Waters with relatively higher TDS were diluted volumetrically prior to analysis. Quantification was performed using seven external calibration standards ranging from 0.1 to 100 ppb. Drift correction was achieved by online addition of 10 ppb of a four element internal standard mix (^{7}Li, Y, Ce, and Bi). An IonPac AS15 2 × 250 mm column was used for anion separation using 38 mM KOH as eluent and ASRS 300 zero reagent suppressor. The sample injection volume was 10 μL and quantification was performed using five external calibration standards ranging from 0 ppm to 10 ppm. Calibration verification standards and blanks were run every 10th analysis for anions and elements. Element analysis was verified with external NIST standard SRM 1643d and anion analysis were verified with a secondary anion standard (Anion II Std Dionex). Samples that exceeded the calibration by 120% were diluted and re-analyzed.

Water samples were analyzed for δ^2H and $\delta^{18}O$ using a Picarro L-1102i WS-CRDS analyzer (Picarro, Sunnyvale, CA) in the ENRI Stable Isotope Laboratory at the University of Alaska Anchorage. International reference standards (IAEA, Vienna, Austria) were used to calibrate the instrument to the VSMOW-VSLAP scale and working standards (USGS45: $\delta^2H = -10.3‰$, $\delta^{18}O = -2.24‰$ and USGS46: $\delta^2H = -235.8‰$, $\delta^{18}O = -29.8‰$) were used with each analytical run to correct for instrumental drift. Long-term mean and standard deviation records of a purified water laboratory internal QA/QC standard ($\delta^2H = -149.80‰$, $\delta^{18}O = -19.68‰$) yield an instrumental precision of 0.93‰ for δ^2H and 0.08‰ for $\delta^{18}O$.

Strontium concentrations and the $^{87}Sr/^{86}Sr$ ratio were measured at the University of Utah Strontium Isotope Geochemistry Laboratory following methods described by Chesson et al. (2012). During the course of analysis measurements of the isotopic standard SRM 987 yielded a value of 0.710301 ± 0.000007 (1σ, n = 51).

Lithium isotopes were all analyzed at Rutgers University by MC-ICPMS following separation using two cation exchange (AGW50x12) columns 200–400 mesh (7 mL resin bed followed by 0.2 mL resin bed) using 0.5 N HCl. A sample of seawater was included with all sample batches and separated using different column pairs to ensure that yields were quantitative. Lithium solutions were analyzed in solutions of 20 ppb concentration, which, utilizing a Teledyne Cetac Aridus II and X-type Ni skimmer cone, yielded a signal exceeding 5-8 V on ^{7}Li with an acid blank of < 150 mV. Standard-sample-standard (L-SVEC) bracketing was used, matching signals to within 5%. A solution of IRMM-016 was included in each batch of analyses, and the long-term δ^7Li average of that, and seawater, were 0.1‰ ± 0.07 (n = 25) and 30.6‰ ± 0.12 (n = 18) respectively.

Dissolved noble gas samples were taken from the halite and marginal nucleus by pumping brine through a copper tube and sealing it with metal clamps. All samples are from brine within 20 m of the salar surface, water levels at these sites ranged from 1.6 to ~15 m below the salar surface. During January of 2012, twenty-one sites were sampled and at one site three depth discrete samples were taken through the upper 10 m of brine with one replicate for the upper most sample (SDA28 series, Table 5). In September of 2012, five sites were

Table 2
Average elemental and isotopic values for each of the five watershed zones by sampling event.

Watershed Zone	Sampling Event	$\delta^{18}O_{VSMOW}$	δD_{VSMOW}	Li	Na	K	Mg	Ca	Cl	SO_4	$^{87}Sr/^{86}Sr$
South		‰	‰	mg/L	mg/L	mg/L	mg/L	mg/L	mg/L	mg/L	
	January 2011										
min		-8.1	-63.7	3.0	526.0	52.5	90.9	165.4	579.5	419.3	0.70726
max		-8.0	-60.9	3.1	587.9	71.5	99.7	167.8	710.3	491.3	0.70802
ave (n = 3)		-8.1	-62.4	3.1	556.5	62.2	95.0	166.8	655.4	458.0	0.70764
	April 2012										
min		-8.1	-65.7	1.2	340.5	32.5	75.7	144.2	402.7	380.8	-
max		-7.7	-63.2	4.4	582.0	71.2	95.2	163.6	915.2	471.2	-
ave (n = 3)		-7.9	-64.6	2.5	444.1	48.1	83.9	151.1	606.2	428.2	0.70750
	September 2012										
min		-8.2	-66.0	1.3	350.6	29.8	70.2	135.6	393.3	405.5	-
max		-7.8	-62.0	3.6	906.0	96.4	91.9	180.2	720.0	517.6	-
ave (n = 3)		-8.0	-64.6	2.4	600.6	65.2	83.5	152.2	562.8	463.1	0.70860
	January 2013										
min		-8.2	-62.6	1.2	312.0	27.9	64.9	90.9	197.6	87.5	-
max		-7.8	-60.9	3.9	547.0	70.7	84.7	168.1	868.9	569.8	-
ave (n = 7)		-8.0	-61.4	2.7	448.1	51.6	75.9	141.8	614.5	430.7	0.70803
	May 2013										
min		-8.7	-60.3	1.1	298.2	26.4	64.8	127.7	237.9	187.1	-
max		-7.6	-54.0	4.4	553.4	67.8	86.6	183.4	789.6	471.0	-
ave (n = 3)		-7.9	-58.3	3.0	460.0	49.0	76.7	153.9	550.2	337.8	-
	January 2014										
min		-8.7	-60.3	2.0	505.5	42.2	81.1	73.1	842.9	495.4	-
max		-7.1	-48.3	4.3	725.5	65.9	117.9	221.8	1267.4	670.1	-
ave (n = 7)		-8.1	-56.4	2.6	621.7	54.5	101.6	166.5	1138.8	568.1	-
	August 2014										
min		-9.0	-63.7	1.1	329.1	30.1	120.2	71.0	319.7	99.0	-
max		-7.5	-52.2	3.4	846.5	83.6	231.5	132.6	1592.2	569.8	-
ave (n = 4)		-8.3	-60.0	2.3	684.5	44.8	174.5	106.0	1006.1	331.4	-
	March 2016										
min		-9.1	-62.3	1.1	248.4	36.7	91.5	64.7	348.3	297.3	-
max		-7.4	-50.3	4.0	796.3	91.9	229.2	112.8	1819.5	593.2	-
ave (n = 6)		-8.4	-58.5	1.9	492.8	63.0	158.1	87.7	1087.5	427.4	-
Southeast											
	June 1993*	-									
min		-		0.2	101.4	11.8	60.9	47.4	88.6	219.5	-
max		-		1.1	763.3	64.9	314.5	130.0	1524.5	768.5	-
ave (n = 3)		-		0.6	444.5	35.2	216.7	85.9	833.1	559.1	-
	October 2011										
min		-8.4	-60.2	0.1	85.2	9.3	39.4	52.1	121.8	320.5	0.70722
max		-8.3	-58.4	1.2	833.4	61.3	151.5	298.9	1433.8	806.5	0.70770
ave(n = 3)		-8.3	-59.3	0.6	442.7	31.5	89.8	212.8	795.2	623.8	0.70753
	January 2012										
min		-8.7	-63.4	0.1	86.3	9.4	40.7	53.3	82.0	183.5	0.70716
max		-8.2	-59.7	1.5	944.7	69.7	172.1	344.3	1527.8	654.0	0.70779
ave(n = 4)		-8.4	-61.0	0.9	620.6	43.3	101.5	230.3	932.1	463.6	0.70758
	April 2012										
min		-8.7	-64.9	0.0	111.8	10.2	32.0	67.3	102.2	204.7	-
max		-8.0	-62.4	1.8	1048.1	76.7	178.3	327.0	1867.5	768.8	-
ave(n = 5)		-8.4	-63.6	1.0	580.1	44.9	92.3	201.7	963.6	440.1	-
	September 2012										
min		-8.4	-63.3	0.8	215.6	10.5	30.5	108.4	366.5	229.1	-
max		-7.6	-54.6	3.4	1075.0	82.2	143.4	274.9	1650.1	713.3	-
ave(n = 4)		-8.2	-60.5	2.4	800.1	60.9	89.9	174.7	1240.1	399.7	-
	January 2013										
min		-8.7	-62.8	0.2	113.7	11.4	29.6	60.7	141.5	221.5	-
max		-7.9	-53.8	1.4	957.3	61.9	148.4	310.9	1732.7	819.5	-
ave(n = 7)		-8.2	-58.5	0.9	515.5	34.4	70.8	176.8	919.9	423.9	0.70781
	May 2013										
min		-9.0	-64.2	0.8	203.2	10.0	29.2	60.8	87.4	186.7	-
max		-7.8	-55.8	1.5	904.9	74.7	162.5	334.8	1949.4	803.3	-
ave(n = 8)		-8.5	-59	1.0	560.8	39.7	89.6	193.8	981.6	407.1	-
	January 2014										
min		-9.2	-64.2	0.6	119.5	11.5	59.4	51.5	126.5	110	-
max		-7.9	-53.1	6.8	1001.9	66.8	281.3	326.5	1671.4	764.3	-
ave(n = 8)		-8.5	-59.5	2.3	757.8	45.4	157.2	143.3	1131.1	457.8	-
	March 2016										
min		-9.3	-63.2	0.2	98.4	12.8	61.6	47.5	101.3	275	-
max		-8.2	-53.2	1.8	1311.5	99.4	490.7	221.9	2607	1387.8	-
ave(n = 10)		-8.6	-59.7	1.2	690.3	73.0	249.8	123.9	1501.2	680.3	-

(*continued on next page*)

Table 2 (*continued*)

Watershed Zone	Sampling Event	$\delta^{18}O_{VSMOW}$	δD_{VSMOW}	Li	Na	K	Mg	Ca	Cl	SO_4	$^{87}Sr/^{86}Sr$
South		‰	‰	mg/L	mg/L	mg/L	mg/L	mg/L	mg/L	mg/L	
Northeast											
	June 1993*										
min		-	-	0.1	40.9	4.9	18.2	7.0	44.3	24.0	-
max		-	-	0.7	259.8	21.0	140.3	130.0	230.4	710.9	-
ave(n = 4)		-	-	0.4	150.4	13.0	79.3	68.5	137.4	367.5	-
	January 2010^										
min		-	-	1.6	317	28.8	26.52	89.4	286.7	221.0	-
max		-	-	0.07	32.3	2.28	5.24	15.4	30.4	44.0	-
ave(n = 2)		-6.3	-50.1	0.8	174.7	15.5	15.9	52.4	158.6	132.5	-
	September 2011										
min		-8.1	-52.7	0.1	31.4	4.6	8.3	21.7	50.3	35.6	-
max		-7.4	-51.2	0.7	291.0	17.1	143.5	141.5	280.9	702.1	-
ave(n = 2)				0.4	161.2	10.8	75.9	81.6	165.6	368.9	0.70772
	January 2012										
min		-9.8	-54.9	0.025	14.7	2.3	9	16.7	29.8	18.3	0.70772
max		-7.3	-52.2	1	308.3	28.1	177.7	207	354.2	1335	0.70790
ave(n = 6)		-8.4	-53.7	0.4	166.8	12.0	72.9	80.8	163.6	451.0	0.70797
	April 2012										
min		-8.2	-61.1	0.8	365.1	38.6	200.2	227.2	370.6	1215.8	-
max		-7.4	-54.7	3.3	941.5	50.9	207.7	479.3	810.6	1667.1	-
ave(n = 2)		-7.8	-57.9	2.0	653.3	44.8	204.0	353.2	590.6	1441.4	-
	January 2013										
min		-7.9	-54.1	0.1	30.1	4.2	7.5	19.6	45.8	51.2	-
max		-7	-51.3	1.1	341.9	36.3	174.7	214.7	382.9	1291.1	-
ave(n = 3)		-7.3	-52.3	0.7	221.6	19.1	106.1	125.7	239.7	696.9	-
	May 2013										
min		-7.9	-53.3	0.1	29.1	4.0	6.0	16.3	33.9	41.0	-
max		-7.4	-50.5	1.3	353.1	38.9	176.9	229.1	368.4	1105.1	-
ave(n = 2)		-7.7	-51.9	0.7	191.1	21.4	91.4	122.7	201.2	573.0	-
	January 2014										
		-7.0	-47.9	0.1	35.0	4.8	17.4	6.7	50.6	34.2	-
	March 2016										
min		-8.4	-55.5	0.1	33.2	4.7	16.1	6.0	41.3	23.2	-
max		-7.9	-52.2	0.7	225.0	24.9	145.7	136.7	230.2	646.8	-
ave(n = 2)		-8.2	-53.9	0.4	129.1	14.8	80.9	71.4	135.8	335.0	-
North											
	June 1993*										
min		-	-	0.3	361.0	14.7	29.4	102.0	547.0	282.0	-
max		-	-	2.5	396.0	37.5	58.3	108.0	547.0	356.0	-
ave(n = 2)		-	-	1.4	378.5	26.1	43.9	105.0	575.5	319.0	-
	January 2010^										
min		-7.1	-57.9	0.4	405.1	14.3	27.9	107.1	577.1	295	0.70756
max		-5.9	-52.1	2.3	432.5	33.7	49.3	108.8	713.4	323	0.70943
ave(n = 2)		-6.5	-55.0	1.4	418.8	24.0	38.6	108.0	645.3	309.0	0.70850
	January 2012										
min		-7.8	-58.3	0.5	455.1	14.5	36.6	117.1	647.3	362.0	0.70750
max		-6.7	-50.9	3.2	627.0	38.6	67.7	155.2	799.8	424.8	0.70926
ave(n = 2)		-7.2	-54.6	1.8	541.1	26.6	52.1	136.2	723.6	393.4	0.70838
West											
	January 2012	-3.2	-49.6	79.7	99849.6	1018.0	848.1	3644.8	132593.3	16052.6	0.70682
	January 2013	-2.9	-46.8	78.6	101215.0	1032.1	835.6	3458.6	159273.5	13944.3	-
	January 2014	-3.8	-49.8	80.3	101713.2	1025.8	827.3	3268.7	121126.2	13587.5	-
average global stream water#				0.003	6.3	2.3	4.1	15	7.8	3.7	
average SDA inflow water				1.5	523.4	42.0	106.0	148.6	797.0	482.7	
SDA inflow enrichment factor				515	83	18	26	10	102	130	
average SdA brine (n = 65)**				1602	78484	19579	12786	4573	165761	25645	

* Risacher et al., 1999.
^ Ortiz et al., 2014.
# Faure (1998).
** Munk et al. (2016b).

resampled (Table 5). In total 29 samples from 21 different sites were analyzed at the University of Utah Dissolved and Noble Gas Laboratory. Gas samples were extracted from the copper tubes and condensed in a stainless steel flask prior to inlet to the mass spectrometry line. Once in the analysis line, a quadrupole mass spectrometer was used to measure Ne, Ar, Kr, and Xe; whereas, He isotopes were analyzed using a magnetic sector mass spectrometer where helium-4 (^{4}He) is measured with a Faraday cup and low abundance helium-3 (^{3}He) is detected with an

Table 3
Sample locations, SC and pH ranges for inflow waters in the five watershed zones.

Region	Sample ID	Water Type	no. samples	latitude	longitude	pH (low-high)	SC (mS/cm) (low-high)
South							
	SDA69	GW	6	-23.80070	-68.23320	6.79-7.62	3.77 - 4.01
	SDA69A	GW	1	-23.80070	-68.23320	7.21	3.60
	SDA69B	GW	1	-23.80070	-68.23320	6.87	3.70
	SDA121	GW	6	-23.80750	-68.22510	6.95-8.54	2.77-4.05
	SDA122	GW	1	-24.01870	-68.21620	7.35	3.7
	SDA138	GW	6	-23.85135	-68.20994	7.19-7.39	2.40-2.58
	SDA138A	GW	1	-23.85135	-68.20994	6.84	2.4
	SDA184	GW	4	-23.80085	-68.22940	7.03-7.77	4.03-4.92
	SDA194	GW	3	-23.75964	-68.18930	7.16-8.03	8.47-29.14
	SDA195	GW	2	-23.74578	-68.19494	7.22-7.45	7.41-9.25
	SDA196	GW	2	-23.77962	-68.16188	7.10-7.25	3.46-3.59
	SDA197	GW	1	-23.77773	-68.18429	8.22	6.56
	SDA197A	GW	1	-23.77773	-68.18429	8.36	8.66
	SDA225	GW	1	-23.79337	-68.12907	8.36	4.69
	SDA226	GW	3	-23.79407	-68.13705	8.02-8.79	4.70-5.28
	SDA227	GW	3	-23.79969	-68.13367	7.07-7.73	4.25-4.67
	SDA228	GW	3	-23.78909	-68.13645	7.52-8.11	4.80-5.85
	SDA276	GW	1	-23.82463	-68.22036	7.52	3.30
Southeast							
	ATA-13*		1	-23.79036	-68.10894	8.42	5.89
	ATA-12*		1	-23.68302	-68.05880	7.54	4.16
	ATA-11*		1	-23.61553	-67.84903	8.72	1.13
	SDA8	SW	10	-23.79036	-68.10894	7.49-8.78	5.86-6.84
	SDA8A	SW	3	-23.79036	-68.10894	7.90-8.23	5.51-6.51
	SDA9	SW	7	-23.68302	-68.05880	7.22-7.87	2.21-4.19
	SDA13	SW	6	-23.61553	-67.84903	6.93-8.96	1.10-1.16
	SDA85	GW	7	-23.77957	-68.11418	7.52-9.74	5.50-6.31
	SDA140	GW	4	-23.47603	-68.04978	7.18-7.47	1.65-2.31
	SDA161	GW	6	-23.77112	-68.11209	7.65-9.33	5.60-6.30
	SDA186	GW	2	-23.49096	-67.98476	7.11-7.29	1.77-1.78
	SDA229	GW	2	-23.74641	-68.11766	8.19-8.74	5.46-5.67
	SDA273	SW	1	-23.79910	-68.08025	7.88	6.34
	SDA274	SW	1	-23.79763	-68.08014	8.01	5.42
	SDA275	SW	1	-23.79591	-68.07660	8.11	10.34
Northeast							
	ATA-6[a]		1	-23.18886	-67.99274	7.77	0.38
	ATA-9[a]		1	-23.32052	-67.78305	6.80	0.60
	ATA-8[a]		1	-23.32392	-67.79430	8.40	1.04
	ATA-10[a]		1	-23.40661	-67.96272	7.08	2.57
	N16[b]	SW	1	-23.25477	-67.98139	NR	1.87
	N14[b]	SW	1	-23.14261	-67.94470	NR	0.20
	SDA5	SW	6	-23.18886	-67.99274	6.38-8.44	0.31-0.50
	SDA7	SW	4	-23.40661	-67.96272	7.79-8.27	2.53-2.72
	SDA76	GW	4	-23.36483	-68.05280	7.08-8.05	2.85-3.34
	SDA78	GW	2	-23.42166	-68.07391	6.90-7.92	2.29-5.17
	SDA86	SW	1	-23.32052	-67.78305	7.21	0.29
	SDA87	SW	1	-23.32392	-67.79430	7.85	0.57
North							
	ATA-4[a]		1	-22.89125	-68.20783	8.00	2.68
	ATA-14[a]		1	-22.86672	-68.18019	7.85	2.85
	E02[b]	SW	1	-22.8283	-68.20639	NR	NR
	N11[b]	SW	1	-22.87051	-68.18916	NR	NR
	SDA134	SW	1	-22.89125	-68.20783	12.06	3.44
	SDA133	SW	1	-22.86672	-68.18019	11.82	2.79
West							
	SDA108	GW	3	-23.5903	-68.57550	6.62-7.35	241-249

NR = not reported.
[a] Risacher et al., 1999.
[b] Ortiz et al., 2014.

electron multiplier. Final values, reported as cubic centimeters per gram at standard temperature and pressure (ccSTP/g), have 2–5% measurement error except for ^{3}He and ^{4}He which have measurement errors of approximately 1%.

3.2. Solids

A preliminary investigation of sediment cores that were extracted from the halite nucleus and from the transition zone over the last few years shows that many of the marginal basin sediment cores contain

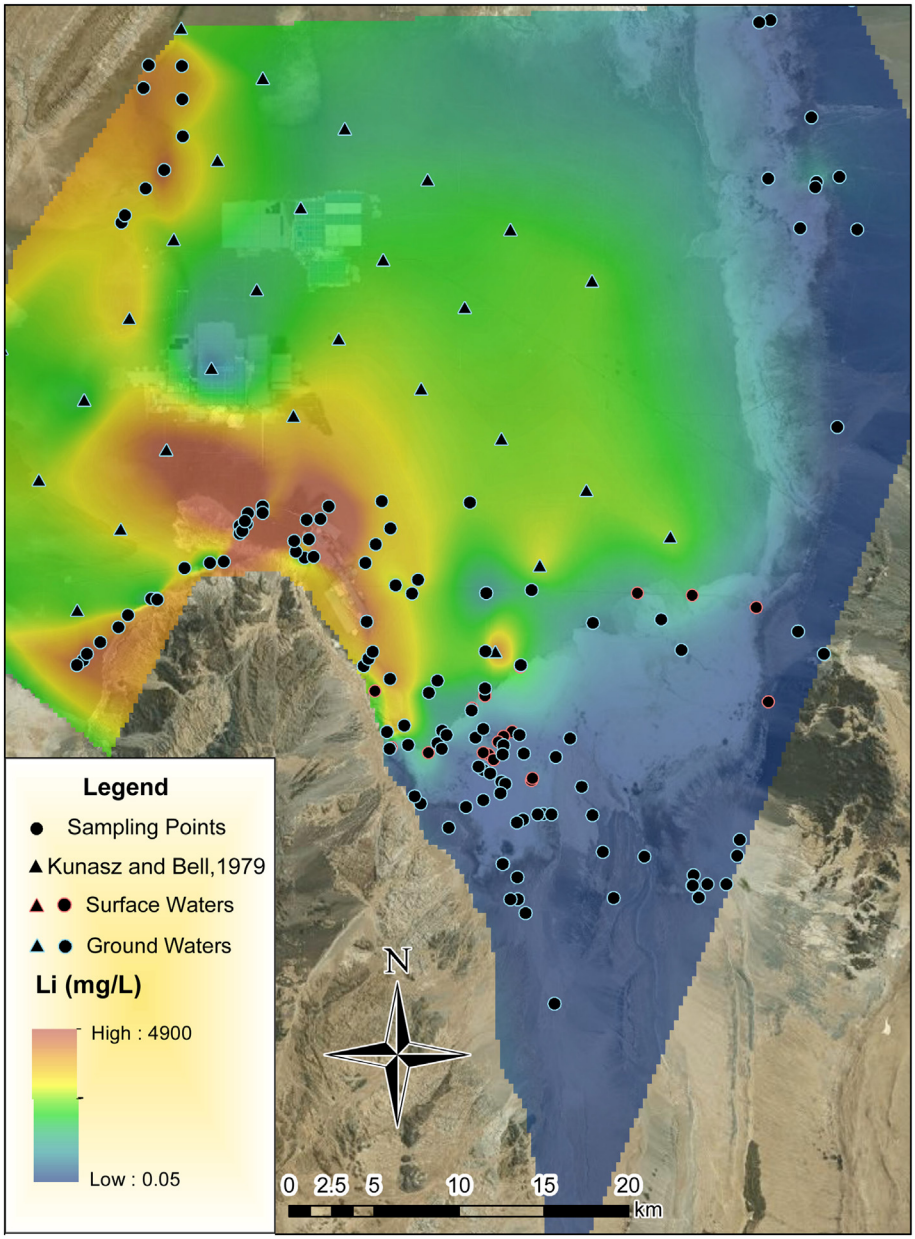

Fig. 2. Lithium concentration distribution map for surface, ground and brine waters from our work (UAA data points) and historical Li concentrations in brine from Kunasz and Bell (1979). Low concentration waters are cooler colors and higher concentrations are warmer. Base map is from Google Earth.

evaporite sequences of carbonate, gypsum and halite with interbedded clay and clastic materials (sand and gravel) and ash and ignimbrite (Munk et al., 2014). Lagoon and shallow lake deposits also exist and are characterized by stromatolites and diatomites. However, the halite nucleus cores distal to the margins are relatively homogenous and composed primarily of halite with minor gypsum. One of these cores (P4, Fig. 1.) used in this analysis is composed of halite over its 60 m length. This core is chosen to represent the relative amounts of Li and other major elements that are held within the solid halite compared to concentrations in the halite-hosted brine. Subsamples of halite from 10 m intervals beginning with 1 m depth to 51 m depth were taken from the P4 core. The lowest part of the core was not sampled as it showed evidence of dissolution from drilling. Each of these subsamples was crushed in an agate mortar and pestle and approximately 2 g of each was dissolved completely in 100 mL of 18 MΩ deionized water. Aliquots of each were pipetted into 15 mL plastic centrifuge tubes and brought to 10 mL volume prior to elemental analysis for Li, K, Ca, and Mg by ICP-MS at the University of Alaska Anchorage using the same methods described above.

Alluvial fan sediment samples were collected for analysis of their bulk Li content and δ^7Li signatures. Two of these samples from representative locations in the basin were bulk sieved in the field and the < 2 mm fraction was retained. This fraction was crushed and pulverized, and a fraction dissolved nearly to completion by a 4 acid method (HF, followed by HNO_3 and $HClO_4$ acids and the final solution brought to volume with a solution of aquaregia) at ACTlabs in Ancaster, Ontario, Canada and analyzed by an Agilent 75 ICP-MS with a detection limit of 1 ppm Li and measured standards were 5% or better accuracy for Li. The Li isotopes were measured at Rutgers University by the same methods described for water samples above following a digestion procedure where 50 mg of powdered rock were digested in savillex vials with HF, HNO_3 and HCl. The solutions were dried, re-dissolved in 0.5 N HCl and loaded onto the columns to yield ~200 ng Li. Rock standards were also analyzed during the time of the run with the following results: JB2 = +5.24 ± 0.7 (n = 8) and JG2 = 1.37 ± 0.7 (n = 14).

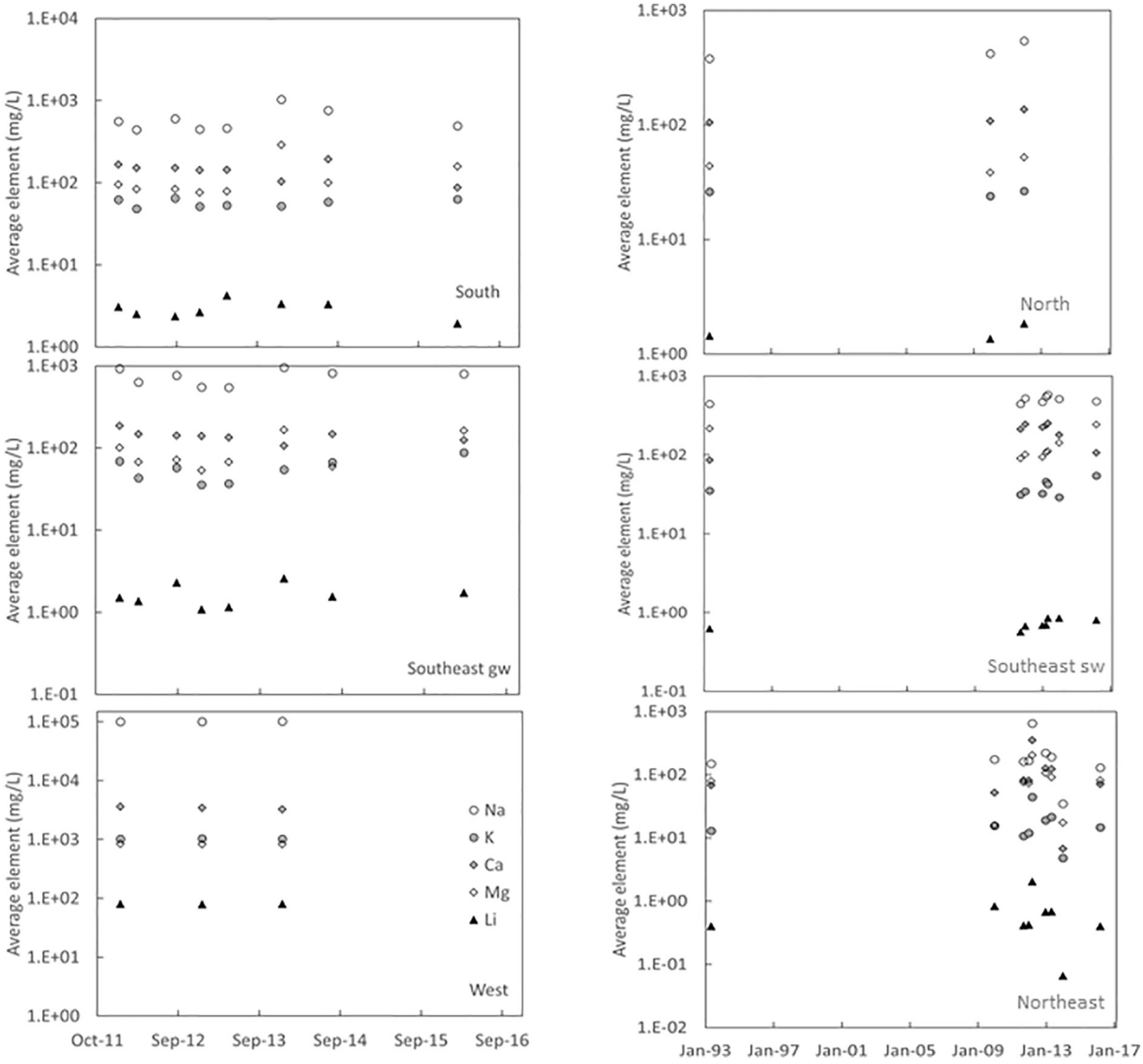

Fig. 3. Time series of average element concentrations from each of the watershed regions (the southeast is divided into surface and groundwater). Historical data from Risacher et al. (1999) is the 1993 data point. In general, the concentrations of Li, Na, K, Ca, and Mg are consistent over the period shown. The northeast region indicates the most variability but that is primarily a function of sample frequency (see text for further explanation).

3.3. Water and elemental fluxes

The topographic watershed of SdA is divided into five sub watersheds/zones (i.e. NE, SE etc.; Fig. 1) for which shallow groundwater inflow and surface water inflows were derived from field observations (Corenthal et al., 2016; Boutt et al., under review). Surface water inflow values were measured at gauging stations by Direccion General de Aguas (2013). Estimates of groundwater inflow were calculated for each sub watershed using general aquifer properties, hydrologic gradients and Darcy's Law (Table S4; Boutt et al., under review). Head values used for these calculations are from Boutt et al. (under review), Salas et al. (2010) and Ortiz et al. (2014). These sub watersheds were further divided into 16 surface and groundwater flux zones used to calculate mass flux to the salar (Fig. 1). These sub-zones were defined by the estimated contributing area of groundwater and/or surface water to a sample site or group of sample sites for which we have measured elemental concentrations. Flux zones are notated SW, GW and SW/GW to indicate the predominant inflow as surface water (SW), groundwater (GW) or having sub-equal proportions of both surface and groundwater (SW/GW). Due to the likelihood that some volume of streamflow is sourced from groundwater and therefore counted twice, these values represent a conservative estimate of the hydrologic balance.

Total inflow through surface water flux zones is determined by the average gauged discharge of all surface water within that zone. For example, inflow in zone SW1 is the average discharge measured at its gauging station near sample site SDA13 (Fig. 1), multiplying this value by the seasonal average measured elemental concentrations at sample site SDA13 gives us a total mass flux from that zone. The total inflow from groundwater flux zones is calculated by distributing the total estimated diffuse groundwater inflow in each sub watershed (i.e. NE, SE) proportionally by the surface area of each zone or its perimeter length at the salar margin. Total diffuse groundwater discharge from the entire SE sub watershed to the salar is assumed to discharge along the length of the interface at the salar margin. By measuring this cross-sectional length in each zone we can distribute the total diffuse groundwater flux proportionally. SW/GW zone fluxes are the summation of groundwater and surface water fluxes in that zone. For example, inflow from zone SW/GW2 was determined by multiplying the ratio of its length along the salar to the total length of the SE sub watershed along the salar by the total diffuse groundwater inflow from the SE sub watershed. This value is added to the surface water inflow within that zone for total

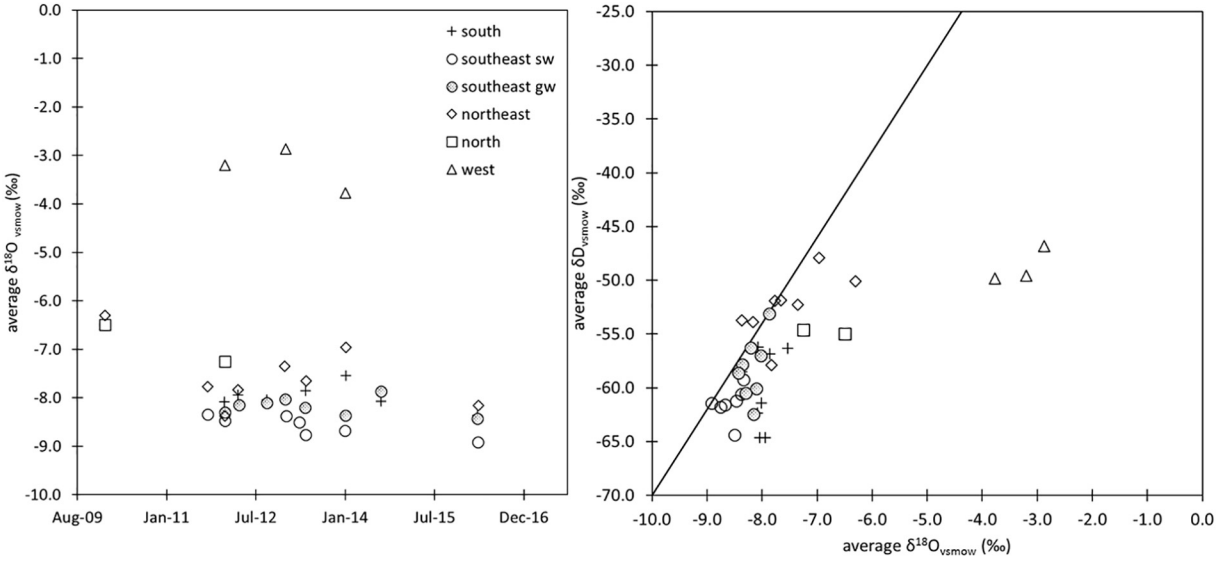

Fig. 4. a–b. The average $\delta^{18}O_{vsmow}$(‰) in waters (a) and average $\delta^{18}O_{vsmow}$ (‰) vs. δD_{vsmow} (‰) in waters (b) with the GMWL shown.

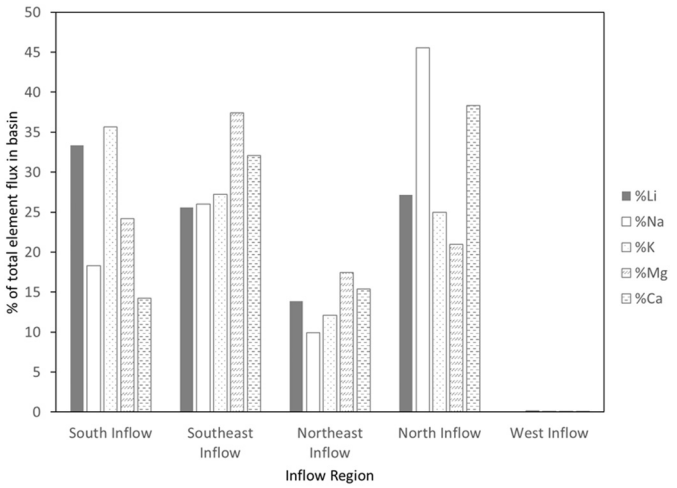

Fig. 5. Percentages of elemental fluxes for each inflow region illustrating the relative contributions of Li, Na, K, Mg, and Ca. Most Li and K are fluxed from the south inflow region while Na and Ca are primarily sourced from the north and Mg is highest in the southeast. The northeast accounts for lesser amounts of these elements and the west contributes less than 1% of all elemental fluxes.

inflow represented by zone SW/GW2. Diffuse groundwater inflow in the NE sub watershed was distributed proportionally among the two groundwater flux zones within it by the relative amounts of surface area extent. Elemental fluxes in the GW and GW/SW sub watersheds are calculated by assigning an average concentration from inclusive sampling sites taken over the period of the study and multiplying that by the respective water flux (Tables 1 and 2).

4. Results and discussion

4.1. Surface and ground water fluxes

Total modern discharge from average surface and groundwater inflows to SdA is estimated to be 4.81 m^3/s, lower than evapotranspiration-based estimated discharge from the basin floor itself (~5.6 to 22.5 m^3/s). Table 1 presents the calculated water fluxes and elemental fluxes for the 16 contributing flux zones encompassing areas from 32 km^2 to 4200 km^2. Fluxes from these zones range from as little as 0.003 m^3/s (SW2 – Rio Camar) to as much as 1.50 m^3/s (SW/GW3 – Rio San Pedro). Four (SW/GW3, SW/GW4, GW2, GW5) out of the 16 flux zones provide 71% of the discharge to the basin. Scaling discharge to watershed area is best fit by a power law described as $Discharge = 0.0023 * Area^{0.6759}$, with an R^2 of 0.382. The lack of a strong correlation between contributing area and discharge is likely due to the role of focused groundwater recharge in higher-elevation portions of the catchments. For example, the San Pedro region provides 31% of the total discharge while comprising 11% of the watershed area. Removing GW1, the diffuse groundwater discharge from the west side of SdA, causes the R^2 to increase to 0.65 highlighting the extremely small contribution of inflow (< 1% - 0.033 m^3/s) from this large (~29% of contributing area) and arid portion of the catchment. These statistics highlight the importance of apportioning solute fluxes to specific subzones within the catchment.

4.2. Lithium distribution in basin waters

Three major types of water in the basin were assigned based on specific conductance (SC) as measured in surface water and shallow (≤ 30 m) groundwater and brines, these include inflow waters (0.1–5 mS/cm) transition zone waters (5–150 mS/cm), and brines (> 150 mS/cm). The inflow waters are used in this study to calculate the elemental fluxes to the basin. The SC and other field parameters are listed in Table 3. Fig. 2 is a Li concentration distribution map which illustrates the complete range of surface and shallow groundwaters in the basin. In general, low Li waters are the inflow waters from the north, east and south upgradient regions, the intermediate Li concentration waters are located in a transition zone along the margin of the halite nucleus where evaporites mixed or interbedded with clays and other detrital material are dominant and punctuated by ash and/or ignimbrite deposits. This marginal environment is characterized by salt cycling (precipitating and dissolving) as a function of dynamic fluctuations in surface and/or shallow groundwater discharge and evapotranspiration. Some of the waters in the transition zone are surface waters that are either channelized, in small lagoons, or open pools which undergo additional evapotranspiration because they are directly exposed to the atmosphere. The highest Li waters (> 1000 mg/L) are high conductivity brines that were sampled primarily from the halite nucleus shallow (< 30 m) aquifer system, margin of the nucleus and the transition zone.

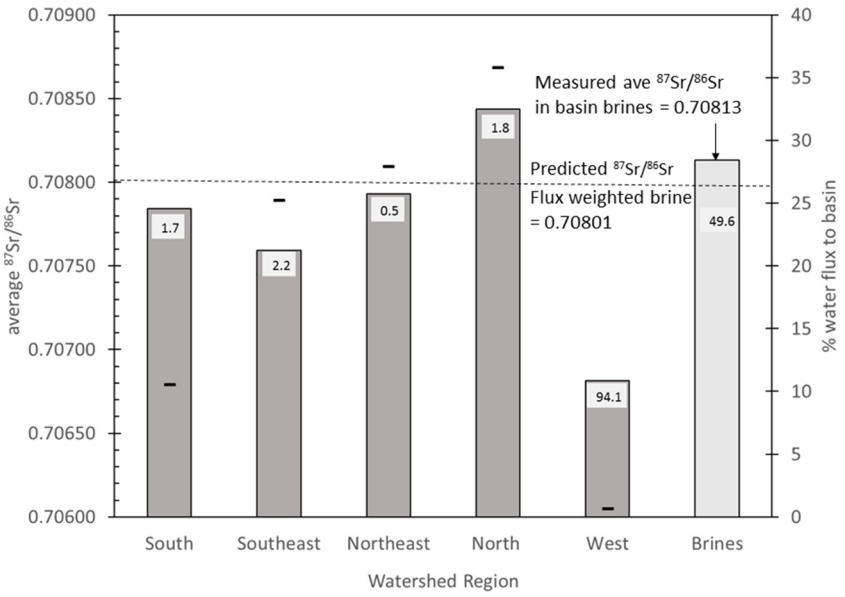

Fig. 6. Average measured and water flux weighted $^{87}Sr/^{86}Sr$ for each watershed inflow region and the southern halite nucleus brines. Relative percent water flux also shown as the dashed data points for each region. Average Sr concentrations shown on each regional bar and for the brines. The flux weighted brine $^{87}Sr/^{86}Sr$ based on relative inflow signatures and associated water flux is close to the average measured $^{87}Sr/^{86}Sr$ of the brines indicating that the inflow water source regions are reasonably representative of brines sampled in the halite nucleus, but that there still may be some sources of water to the nucleus brines that are unaccounted for.

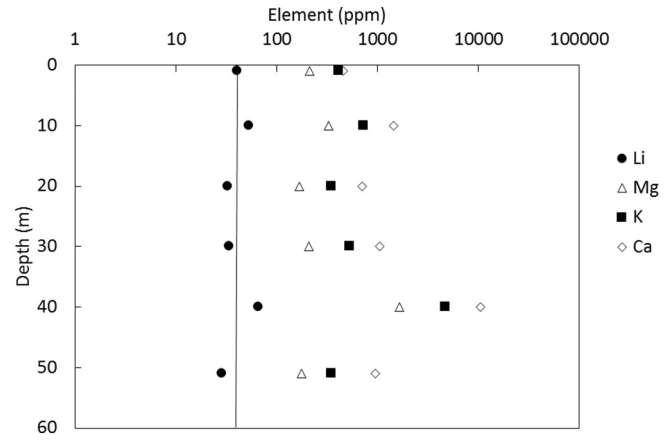

Fig. 7. P4 core (location shown in Fig. 1) major element concentrations as a function of depth indicating an average Li concentration of approximately 40 ppm over the 50 meters of the predominantly halite core. Other major elements vary systematically with depth.

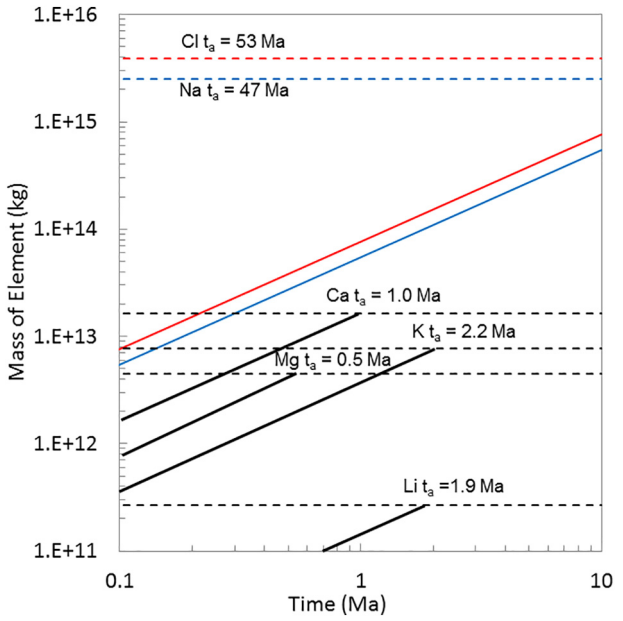

Fig. 8. Mass accumulation and balance of major elements and Li as a function of time based on calculated masses of each in the nucleus brines and halite aquifer material.

4.3. Elemental and isotopic composition over time

The average, minimum and maximum major element concentrations, $\delta^{18}O$ and δD for water, as well as the average $^{87}Sr/^{86}Sr$ signatures were determined for each region (Table 2). Averages are used in the solute flux calculations in order to assign a reasonable single value to each region given the extensive seasonal and multi-year data set.

Seasonal changes in the average elemental concentrations over the six- year period of the study are investigated to establish any variations in chemical composition of the inflow waters that may impact the averages used to calculate elemental fluxes (Fig. 3). In general, the Li, Na, K, Ca, and Mg concentrations in each of the five inflow regions are consistent (within the same order of magnitude) over time. In the case of the San Pedro River in the north region as well as in the southeast surface water region we also include a sampling event from June 1993 (Risacher et al., 1999) the results of which are consistent with the more recent sampling in both of these regions over two decades later. Also, included in the elemental averages for the north and northeast regions is a January 2010 sample site from Ortiz et al. (2014). No $\delta^{18}O$ or δD values for water were reported in Risacher et al. (1999) but Ortiz et al. (2014) did report $\delta^{18}O$ for some sampling events and one site was relevant to our work and is included in our analysis. These results establish the consistency of major cation concentrations in inflow waters to the basin over at least the period of this study and even over the past two decades for some sites suggesting that the average elemental concentrations we use to characterize surface and shallow groundwater fluxes to the basin are representative of at a minimum the modern environment. The northeast inflow region appears to have the most variability in elemental concentrations but this is primarily reflected in two of the sampling events. The April 2012 sampling event was based on two shallow groundwater sites and one (SDA78) is located along the margin between alluvial fans and the transition zone on the east side of the basin and it had an SC value close to our high end cutoff (5.0 mS/cm) for inflow water classification of 5.168 and therefore the elemental concentrations are on the high end of our inflow water data set. On the other hand, the January 2014 sampling event is based only on the surface water at site SDA5 which is on the very low end of SC waters for this inflow region with a value of 0.305–0.490 mS/cm. Although all of

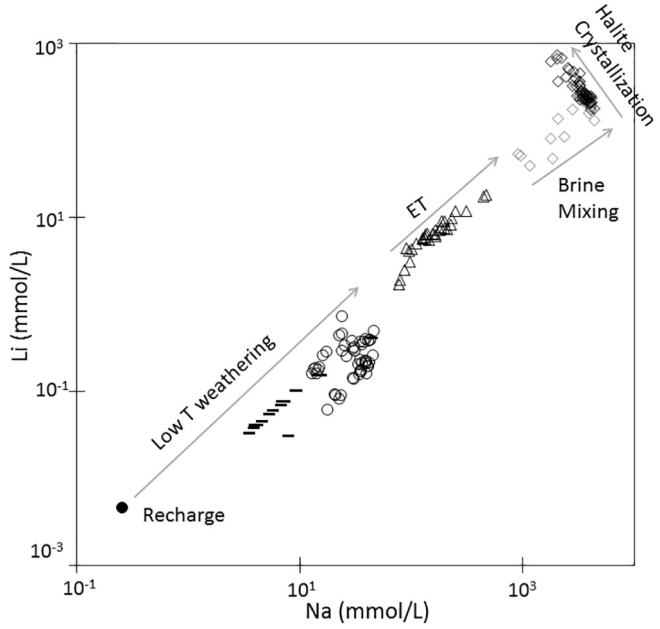

Fig. 9. Geochemical evolution of inflow waters to brines for the Salar de Atacama basin. Recharge waters are considered to be precipitation in the basin (solid circle), infiltrated waters in the shallow subsurface or surface flows indicate low T weathering is likely responsible for increased Li to the waters, perhaps along two distinct flow paths (solid dashes data from the MNT aquifer (Rissmann et al., 2015), open circles from this study), followed by evapotranspiration concentration in the transitional zones of groundwater discharge (open triangles), brine mixing in the transition zones outside of the halite nucleus (open gray diamonds) and finally halite crystallization (removal of Na) drives the Li concentration to the highest values in the halite nucleus brines (open black diamonds).

these sampling locations are within the inflow region these examples further exemplify why using elemental averages to determine elemental fluxes for each region are justified in order to dampen the low and high end SC waters as well as the fact that there is variability in the number of sites sampled during each event.

A comparison of the average elemental concentrations in the inflow waters from each sub watershed to that of global stream water is included in Table 2. The relative enrichment of each element is calculated by dividing the average elemental concentration of all the inflow waters to the SdA by the average global stream water concentrations. Lithium is enriched by a factor of 515, Na by 83, Mg by 26, K by 18, Ca by 10 and SO_4 by 130 and Cl by 102. This is an important observation as it indicates that the inflow waters of this basin are already enriched in these elements before they enter the closed system where further hydrogeochemical processes alter their concentrations in fluids.

Fig. 4a–b illustrates the average $\delta^{18}O$ of inflow waters as a function of time (a) and the average $\delta^{18}O$ vs. δD of waters for the same sites (b) from each of the five regions. These data indicate a consistent pattern over the period of the study with only a small < 1–2‰ range, similar to the consistent elemental concentrations in the inflow regions. However, the $\delta^{18}O$ and δD of the waters also indicate that there are varied inflow water types originating from different sources in the recharge zones. For example, it is evident that the north and northeast inflow waters appear to have a more enriched $\delta^{18}O$ and δD signature as compared to the inflow waters in the southeast and south. Additionally, the southeast surface waters are generally depleted as compared to the southeast shallow groundwater with some overlap in signatures. This is likely indicative of differing and/or mixed sources of recharge to these areas. The waters in the west zone are likely very old as there is almost no recharge in this region and the groundwaters sampled have high TDS, probably representative of mixed recharge and ancient brine resulting in a relatively enriched $\delta^{18}O$ signature.

4.4. Regional elemental fluxes and sources of water

Regional elemental fluxes of Li, Na, K, Ca, and Mg were calculated as percentages (Fig. 5) in order to define the relative contributions from

Table 4
Lithium and δ^7Li for potential Li source rocks and associated leachates.

Sample	Li (ppm)	δ^7Li (‰)	Li_l/Li_r *100	dif. δ^7Li (‰)	source
Lascar Volcano, Salar de Atacama, Chile (1993 eruption)					
LAS-S rock	NA	NA			Risacher and Alonso, 2001
LAS-S leach	0.078 (480 min)	NA			
LAS-W rock	NA	NA			
LAS-W leach	0.22 (480 min)	NA			
LAS-V rock	NA	NA			
LAS-V leach	0.24 (600 min)	NA			
LAS-S rock	22.7	+3.1	1.32		Godfrey et al., 2013
LAS-S leach	0.3	ND			
LAS-W rock	15.8	+2.0	7.59	5.60	
LAS-W leach	1.2	+7.6			
Salar de Hombre Muerto, Argentina					
SHM rock	24.56	+7.2	2.85	5.40	
SHM leach	0.7	+12.6			
Clayton Valley, Nevada, USA					Jochens and Munk, 2011 and this study
CV2R rock	21.4	-5.19	0.05	7.31	
CV2R leach	0.01	+2.12			
10DW21 fan	4.5	-1.90	0.33		
10DW21 leach	0.015	NA			
10DW22 fan	14	-1.99	0.36	7.63	
10DW22 leach	0.05	+5.64			

Li_l/Li_r * 100 is equivalent to the concentration of Li in the leachate divided by the concentration in the rock multiplied by 100.
dif. δ^7Li (‰) is the absolute ‰ difference between the rock and the leachate.

Table 5
Dissolved noble gases in SdA marginal and nucleus brines.

Sample ID	brine type	sample date	SC	R/Ra*	He^4	Ne	Ar	Kr	Xe
			(mS/cm)		(ccSTP/g)	(ccSTP/g)	(ccSTP/g)	(ccSTP/g)	(ccSTP/g)
SDA14W	nucleus	1/7/12	237	1.04	8E-09	2E-08	3E-05	6E-09	7E-10
SDA19W	nucleus	1/7/12	222	0.98	7E-09	3E-08	3E-05	5E-09	7E-10
SDA28W	nucleus	1/6/12	233	1.12	8E-09	3E-08	3E-05	7E-09	9E-10
SDA28W-s	nucleus	1/7/12	233	1.08	8E-09	3E-08	3E-05	5E-09	8E-10
SDA28W-m	nucleus	1/7/12	234	1.15	8E-09	3E-08	3E-05	5E-09	8E-10
SDA28-d	nucleus	1/7/12	231	1.10	9E-09	3E-08	3E-05	6E-09	8E-10
SDA29	nucleus	1/7/12	232	0.79	2E-08	1E-08	2E-05	5E-09	6E-10
SDA29	nucleus	9/25/12	231	0.82	3E-08	2E-08	2E-05	6E-09	7E-10
SDA30	nucleus	1/7/12	235	1.27	6E-09	1E-08	2E-05	5E-09	7E-10
SDA30	nucleus	9/25/12	221	1.17	8E-09	2E-08	3E-05	7E-09	8E-10
SDA94	nucleus	1/7/12	236	1.27	7E-09	2E-08	3E-05	6E-09	9E-10
SDA97	nucleus	1/8/12	242	0.85	1E-08	3E-08	3E-05	4E-09	7E-10
SDA98	nucleus	1/8/12	249	0.98	7E-09	2E-08	3E-05	5E-09	7E-10
SDA99	nucleus	1/8/12	221	0.13	8E-08	2E-08	2E-05	4E-09	5E-10
SDA99	nucleus	9/28/12	221	0.13	7E-08	2E-08	2E-05	5E-09	7E-10
SDA102	nucleus	1/9/12	246	1.01	3E-09	7E-09	9E-06	2E-09	3E-10
SDA105	nucleus	1/9/12	233	0.98	1E-08	3E-08	3E-05	6E-09	7E-10
SDA107	nucleus	1/9/12	238	0.89	9E-09	2E-08	3E-05	6E-09	8E-10
SDA108	nucleus	1/12/12	241	0.21	6E-07	1E-08	1E-05	2E-09	4E-10
SDA108	nucleus	9/27/12	243	0.18	7E-07	2E-08	1E-05	3E-09	3E-10
SDA109	marginal	1/10/12	241	1.15	8E-09	3E-08	4E-05	8E-09	1E-09
SDA111	marginal	1/10/12	243	1.04	9E-09	3E-08	4E-05	9E-09	1E-09
SDA112	marginal	1/10/12	241	1.06	8E-09	3E-08	4E-05	9E-09	1E-09
SDA116	nucleus	1/11/12	237	0.03	1E-06	3E-08	3E-05	4E-09	6E-10
SDA117	nucleus	1/11/12	240	0.02	2E-06	2E-08	2E-05	3E-09	4E-10
SDA117	nucleus	9/27/12	236	0.02	2E-06	2E-08	3E-05	7E-09	8E-10
SDA118	nucleus	1/11/12	240	0.02	1E-06	2E-08	3E-05	5E-09	8E-10
SDA119	nucleus	1/11/12	231	0.97	1E-08	3E-08	3E-05	5E-09	7E-10
SDA120	nucleus	1/11/12	237	0.80	9E-09	2E-08	2E-05	5E-09	8E-10

*$^3He/^4He$ ratio of dissolved gas in brine reported relative to the atmosphere using a $^3He/^4He$ ratio of 1.38E-06 (Ra). Locations of nucleus brines is proprietary information. Locations of the three marginal brines are available in Table 6.

each of the five watershed regions. Lithium flux is highest from the south inflow region which contributes about 33% of the total Li to the basin. This is followed by the north region contributing 27%, the southeast 25%, and the northeast 14%. The west region contributes < 1% of all element fluxes primarily due to the very low water flux, specifically 0.06% Li comes from the west inflow region. Consistent with the water flux numbers, over half of the Li fluxing to the basin comes from the south and southeast (a combined total of 60%). Sodium mass flux is highest from the north region at 47%, followed by the southeast and south at 20.5% and 19.3% respectively and 39.8% combined, the northeast at 13.2% and the west region contributes the smallest amount at 0.19%. The observation that the majority of Na is contributed from the north whereas for Li it is from the south and southeast allows us to begin to understand that the relative sources/inputs of these two elements is not necessarily the same.

Potassium mass flux is 38.5% from the south followed by 26.3% from the north region, 20.5% from the southeast, 10.2% from the northeast and 0.03% from the west. The combined south and southeast contributions are 58.7%. The calcium mass flux is 39.1% from the north inflow region, 27.7% from the southeast, 15.8% from the northeast, 14.8% from the south and 0.02% from the west. In this case the north and south regions are contributing about equal amounts of Ca to the basin and the combined total from the south and southeast is 42.4%. Magnesium mass fluxes are the most similar across the four main contributing regions compared to any other solute. Twenty-eight percent is sourced from the south followed by 26.6% from the southeast, 24.3% from the north, 20.2% from the northeast and the lowest from the west at 0.01%. A combined total of 54.6% from the south and southeast regions. In summary, the south and southeast regions when combined are responsible for contributing the majority of Li (60%), K (58.7%), Mg (54.6%), and Ca (54.6%), whereas the north and southeast combined contribute most of the Na (67.5%).

In order to further investigate the relative contributions of water flux weighted solutes to the basin, $^{87}Sr/^{86}Sr$ in surface and shallow groundwaters weighted by the relative water fluxes were evaluated. On a first order the $^{87}Sr/^{86}Sr$ signatures of inflow waters and halite nucleus brines can indicate if the water sources represented in the analysis are a reasonable estimation of water and solutes entering and accumulating in the basin at least in the shallow (< 30 m) part of the halite nucleus aquifer where we have access to brine samples. The average $^{87}Sr/^{86}Sr$ signatures of inflow waters to the SdA basin range from the least radiogenic waters in the west with 0.70682 to the most radiogenic waters in the north with 0.70844, and the average $^{87}Sr/^{86}Sr$ of brines sampled in the halite nucleus is 0.70813 (n = 25) (Fig. 6). Rissmann et al. (2015) indicate an average $^{87}Sr/^{86}Sr$ for higher elevation inflow waters (higher in the recharge zone) from the major aquifer (MNT) in the south that is 0.70740. This value is lower than our average south (0.70784) and southeast (0.70759) averages for shallow groundwater and surface waters but closer to what we measure for the southeast, indicating that there are other sources of water contributing in the south. Ortiz et al. (2014) report $^{87}Sr/^{86}Sr$ values for some inflow waters (ground and surface) as well as lagoon waters for the northeast region of the basin and similar to our study their values are more radiogenic, although their average value is a bit higher (closer to 0.709) whereas ours is closer to 0.708.

The calculated water flux weighted $^{87}Sr/^{86}Sr$ of the brines based on the average regional inputs is estimated at 0.70801 as compared to the average measured $^{87}Sr/^{86}Sr$ in brines of 0.70813. This indicates that the weighted flux average is slightly less radiogenic than what was measured in the brines and that although there is a close match there are likely still some unaccounted sources of water and solutes to the basin brines that have not been captured.

Table 6
Lithium and δ^7Li for waters in the SdA basin.

Sample ID	Water type	latitude	longitude	Li (mg/L)	δ^7Li (‰)
SDA13	inflow	-23.61553	-67.84903	0.1	5.3
SDA9*	inflow	-23.68302	-68.05880	0.6	9.4
SDA138*	inflow	-23.85135	-68.20994	1.2	4.4
SDA85*	inflow	-23.77957	-68.11418	1.8	5.8
SDA121	inflow	-23.80750	-68.22510	3.0	7.3
SDA69	inflow	-23.80070	-68.23320	3.1	6.8
SDA71	inflow	-23.75595	-68.25669	7.1	7.0
SDA74	inflow	-23.76355	-68.22979	8.7	7.4
SDA32	inflow	-23.75073	-68.28339	10.8	9.3
SDA72	transition	-23.75268	-68.24754	13.2	8.3
SDA75	transition	-23.73188	-68.20920	16.7	10.4
SDA34	transition	-23.73493	-68.25166	23.4	8.9
SDA70	transition	-23.78997	-68.22953	33.2	9.2
SDA73	transition	-23.74944	-68.23846	43.5	8.5
SDA37*	lagoon	-23.73302	-68.24202	82.7	10.1
SDA141*	lagoon	-23.68019	-68.14596	319.0	10.9
SDA35*	lagoon	-23.73065	-68.24490	353.9	10.9
SDA36*	lagoon	-23.72984	-68.24763	533.9	11.6
SDA118	marginal brine	-23.66200	-68.52610	442.0	10.4
SDA111	marginal brine	-23.69565	-68.24459	593.1	11.8
SDA135	marginal brine	-23.69990	-68.30479	683.5	10.7
SDA112	marginal brine	-23.69857	-68.24658	721.1	10.9
SDA109	marginal brine	-23.68743	-68.22783	895.1	10.5
SDA113	marginal brine	-23.69480	-68.27170	1090.4	10.1
SDA110	marginal brine	-23.68054	-68.24639	1205.9	9.6
SDA94	nucleus brine	-	-	1177.5	10.5
SDA15	nucleus brine	-	-	1464.7	11.5
SDA28	nucleus brine	-	-	1537.1	10.3
SDA30	nucleus brine	-	-	1689.8	11.4
SDA21	nucleus brine	-	-	1714.3	10.8
SDA29	nucleus brine	-	-	1715.7	11.8
SDA128	nucleus brine	-	-	1717.8	10.4
SDA39	nucleus brine	-	-	1866.9	10.2
SDA22	nucleus brine	-	-	1967.6	11.3
SDA115	nucleus brine	-	-	2363.9	12.6
SDA114	nucleus brine	-	-	2488.6	11.4
SDA20	nucleus brine	-	-	4626.0	11.0
SDA19	nucleus brine	-	-	5092.2	10.0

Samples from January 2012 sampling campaign except those noted *from April 2012 sampling campaign. Locations of nucleus brines is proprietary information.

4.5. Solute mass balance

As previously documented by Corenthal et al. (2016) the minimum long-term water discharge required to sustain halite accumulation with a balanced water budget for SdA is similar to the estimated timing of 6–10 Ma for halite accumulation based on geological constraints (Jordan et al., 2002a, 2002b, 2010). Such a scenario yields modern water fluxes to the basin that are 9–20 times greater than modern recharge within the topographic watershed, and thus relies upon regional groundwater flow from the adjacent Central Andean Plateau (cf. Corenthal et al., 2016). This suggests additional water and solute sources are required to explain the thick accumulation of salts. Here we explore this hypothesis further by expanding the number of elements investigated, using the observed modern solute fluxes, and comparing these to newly reported data on the elemental composition of brine and of halite from a sediment core extracted from the halite nucleus.

Fig. 7. illustrates the concentration of Li, K, Ca, and Mg as a function of depth in the P4 halite core which was extracted from the halite nucleus (Fig. 1). This analysis is important for calibrating the amount of Li contained in the halite nucleus because the mass of Li in halite plus the mass of Li in the brines is the best estimate of total Li accumulated in the basin. Analysis of halite from this core indicates that there is an average of ~40 ppm Li within halite crystals in the halite nucleus. Lithium and the other elements analyzed vary systematically with depth. Once the brines reach halite saturation (which is the case for the shallow halite nucleus brines) any other remaining ions in solution that are not forming solids may be trapped as fluid inclusions or forced into the brine phase. The process of halite crystallization appears to play an important role in the final concentration of Li and other elements in the brines (Fig. 9) and ultimately the formation of the Li brine ore deposit.

Fig. 8 illustrates the projected time it would take to accumulate the mass of Li, K, Na, Ca, Mg and Cl in the halite nucleus brine and halite/evaporite aquifer based on the modern water and solute fluxes used in this study and the estimated volume of salts and brine in the basin from Corenthal et al. (2016). The mass of elements in the halite is determined from the analysis of the 60 m P4 halite core and the mass of elements contained in the brine is derived from a set of 65 brine samples (Table 2) from the brines in the basin. Here we build on the original hypothesis tested in Corenthal et al. (2016) where the accumulation time was set at the maximum estimate of 10 Ma by using an approach in which we have further refined the water and elemental fluxes and we let the modern inflow regime dictate the time to accumulate each element.

Lithium, K, Ca and Mg appear to balance on shorter time scales of 0.5 Ma (Mg), 1.0 Ma (Ca), 1.9 Ma (Li) and 2.2 Ma (K) as compared to 47 Ma (Na) and 53 Ma (Cl). This difference is most likely explained through the starting composition of the inflow waters, addition of solutes through weathering, recycling of secondary salts from high elevation lakes and/or older salars, and the geochemical behavior and properties of these elements along flow paths. Table 3 shows the average inflow water concentrations for these elements and their relative enrichment factors in the SdA basin inflow waters as compared to average global stream water. These concentrations suggest that there are particularly elevated concentrations of Na and Cl already contained in the inflow waters to the basin. For example, Grosjean (1994) showed that Laguna Lejia (a high elevation lake on the Altiplano, Fig. 1) is not accumulating halite despite rapid turn-over rates indicating losses of solutes to the groundwater, particularly the more conservative solutes such as Cl and Na. However, another high elevation lake on the Altiplano (Laguna Tuyajto, Fig. 1) is actively precipitating halite and is considered to be a closed-basin (Herrera et al., 2016). Rissmann et al. (2015) have demonstrated that it is possible that there are sources of solutes in the south and southeast parts the SdA basin which originate from the weathering of older evaporite deposits, therefore this could be an important mechanism responsible for the elevated Na and Cl concentrations given that NaCl is highly soluble and therefore easily mobilized. Additionally, if we compare the $^{87}Sr/^{86}Sr$ values of high elevation lakes including Laguna Lejia (0.70760, this study), Laguna Tuyajto (0.70815, this study), Laguna Miniques (0.70714, from Boschetti et al., 2007, Fig. 1) to the average brines in the SdA (0.70813) it is evident that the $^{87}Sr/^{86}Sr$ signature of the brines is most like that of Laguna Tuyajto (also one of the highest Li concentrations is found in this lake), however, this does not preclude the potential for other sources of water along flow paths from the Altiplano to the SdA. For example, the Li concentrations of Laguna Lejia, Laguna Tuyajto and Laguna Miniques are 56.4 mg/L, 297.4 mg/L, and 1.5 mg/L respectively, however, the relative contributions of these potential sources to the overall Li flux is not currently known. Further investigation of the possible connections between the high elevation lakes and the water and solutes that reach the SdA basin is necessary to unravel the relative contributions of these water bodies. Nevertheless, the possibility of water and solute contributions from high elevation lakes is consistent with our observations that additional water and solute sources outside what is observed in the modern are required to balance the Na and Cl budgets within the estimated timeframe of the halite nucleus formation.

In terms of the relative conservative behavior of the major elements and their relationship to the geochemical processes occurring in the discharge zones (transition zone) there is a recognizable and consistent pattern such that Ca and Mg appear to be removed in carbonate, sulfate and chloride phases in the marginal zones of the halite nucleus. These secondary salts have been observed in the field by our team and are also documented by Ide and Kunasz (1989) and McCartney (2001). Lithium

Table 7
Lithium and Na concentrations for waters in SdA.

Sample ID	Water type	Sample Date	latitude	longitude	Li (mmol/L)	Na (mmol/L)
SDA190	rain	5/17/2013	-23.68183	-68.06730	0.01	0.2
SDA220	rain	1/17/2014	-23.78762	-67.85493	0.002	0.3
MPW-11	inflow gw	NR	-24.21278	-68.29170	0.04	3.9
MPW-8	inflow gw	NR	-24.20645	-68.29397	0.04	4.2
MPW-5	inflow gw	NR	-24.18829	-68.27898	0.03	3.6
MPW-21	inflow gw	NR	-24.19761	-68.29397	0.04	4.0
MPW-4	inflow gw	NR	-24.18876	-68.29674	0.05	4.7
MPW-10	inflow gw	NR	-24.21299	-68.30123	0.1	7.5
MPW-2	inflow gw	NR	-24.17918	-68.29828	0.1	6.9
MPW-3	inflow gw	NR	-24.17922	-68.28419	0.1	5.8
MPW-7	inflow gw	NR	-24.19667	-68.28403	0.1	7.1
MPW-13	inflow gw	NR	-24.22264	-68.29111	0.1	5.4
MPW-14	inflow gw	NR	-24.22637	-68.29959	0.0	8.0
MPW-15	inflow gw	NR	-24.23220	-68.30257	0.1	9.4
MPW-9	inflow gw	NR	-24.22584	-68.33104	0.4	45.2
MPW-18	inflow gw	NR	-24.26108	-68.36017	0.2	15.9
MPW-17	inflow gw	NR	-24.26137	-68.37140	0.1	9.4
MPW-19	inflow gw	NR	-24.27467	-68.37629	0.1	9.3
MPW-20	inflow gw	NR	-24.27082	-68.36547	0.2	14.7
SDA122	inflow gw	1/11/2012	-24.01870	-68.21620	0.4	24.2
SDA138A	inflow gw	1/12/2013	-23.85135	-68.20994	0.2	14.1
SDA138	inflow gw	4/2/2012	-23.85135	-68.20994	0.2	14.8
SDA138		9/29/2012			0.2	15.3
SDA138		1/12/2013			0.2	13.6
SDA138		5/16/2013			0.2	13.0
SDA138		1/9/2014			0.2	14.3
SDA121	inflow gw	1/11/2012	-23.80750	-68.22510	0.4	22.9
SDA121		4/2/2012			0.3	17.8
SDA121		1/12/2013			0.3	16.4
SDA121		1/9/2014			0.3	25.7
SDA8A	inflow sw	1/12/2012	-23.80001	-68.09796	0.2	41.1
SDA8	inflow sw	10/1/2011	-23.79036	-68.10894	0.2	36.3
SDA8		4/8/2012			0.2	42.7
SDA8		9/25/2012			0.4	39.6
SDA8		1/13/2013			0.2	35.8
SDA8		5/14/2013			0.2	35.5
SDA8		5/18/2013			0.2	39.3
SDA8		1/9/2014			0.2	40.3
SDA85	inflow gw	1/14/2012	-23.77957	-68.11418	0.2	40.1
SDA85		4/8/2012			0.3	45.6
SDA85		9/25/2012			0.4	43.5
SDA85		1/12/2013			0.2	41.6
SDA85		5/14/2013			0.2	37.1
SDA85		1/9/2014			0.4	42.3
SDA161	inflow gw	9/29/2012	-23.77112	-68.11209	0.5	46.8
SDA161		1/12/2013			0.2	39.4
SDA161		1/13/2013			0.2	33.9
SDA161		5/14/2013			0.2	39.4
SDA161		1/14/2014			0.4	43.6
SDA161		8/18/2014			0.2	35.3
SDA225	inflow gw	1/19/2014	-23.79337	-68.12907	0.3	36.8
SDA226	inflow gw	1/19/2014	-23.79407	-68.13705	0.4	35.3
SDA226		8/18/2014			0.3	31.6
SDA227	inflow gw	1/19/2014	-23.79969	-68.13367	0.4	29.9
SDA227		8/18/2014			0.3	24.2
SDA228	inflow gw	1/19/2014	-23.78909	-68.13645	0.3	30.9
SDA228		8/18/2014			0.3	30.4
SDA229	inflow gw	1/19/2014	-23.74641	-68.11766	0.4	38.4
SDA230	inflow gw	1/14/2014	-23.80002	-68.17868	0.2	26.6
SDA9	inflow sw	10/1/2011	-23.68302	-68.05880	0.1	17.9
SDA9		1/12/2012			0.1	23.0
SDA9		4/8/2012			0.1	23.8
SDA9		1/21/2013			0.1	20.7
SDA9		5/19/2013			0.1	21.3
SDA2	inflow gw	9/30/2011	-23.67112	-68.08096	0.1	30.3
SDA2		1/12/2012			0.1	31.3
SDA2		4/8/2012			0.2	34.7
SDA200A	transition inflow gw	8/16/2014	-23.78372	-68.23718	0.7	24.1
SDA72	transition inflow gw	1/12/2012	-23.75268	-68.24754	1.9	79.0
SDA72		9/27/2012			2.5	86.7
SDA72		1/13/2013			1.7	78.4
SDA72		5/15/2013			3.0	97.5
SDA149	transition inflow gw	4/5/2012	-23.73115	-68.24692	7.6	198.0
SDA149		9/28/2012			4.1	96.1

(*continued on next page*)

Table 7 (*continued*)

Sample ID	Water type	Sample Date	latitude	longitude	Li (mmol/L)	Na (mmol/L)
SDA149		1/13/2013			5.4	145.7
SDA149		8/11/2014			6.0	130.5
SDA37	lagoon inflow gw	10/3/2011	-23.73302	-68.24202	7.3	209.4
SDA37		4/5/2012			11.9	311.8
SDA37		9/28/2012			7.7	185.4
SDA37		1/13/2013			7.1	182.0
SDA37		5/15/2013			4.4	90.8
SDA37		1/11/2014			7.2	163.4
SDA37		8/11/2014			9.2	189.6
SDA172	lagoon inflow gw	10/2/2012	-23.72181	-68.23693	4.3	101.8
SDA172		8/12/2014			4.9	110.9
SDA171	lagoon inflow gw	10/2/2012	-23.71958	-68.23218	5.6	126.9
SDA171		1/13/2013			17.2	444.8
SDA171		5/15/2013			11.9	250.8
SDA171		1/11/2014			18.0	470.2
SDA171		8/12/2014			9.0	197.7
SDA171A	lagoon inflow gw	1/13/2013	-23.71969	-68.23171	6.4	165.0
SDA173	lagoon inflow gw	10/2/2012	-23.72447	-68.23954	5.6	134.7
SDA173		1/13/2013			8.2	226.8
SDA173		5/15/2013			6.5	139.0
SDA173		1/11/2014			9.7	231.3
SDA173		8/12/2014			6.3	134.5
SDA172	lagoon inflow gw	1/13/2013	-23.72181	-68.23693	6.0	164.5
SDA172		5/15/2013			5.8	126.5
SDA172		1/11/2014			6.5	157.0
SDA154	transitional brine	1/15/2013	-23.70837	-68.27513	85.4	2374.1
SDA213	transitional brine	1/14/2014	-23.65091	-68.22198	159.6	3949.9
SDA213		8/16/2014			53.6	911.4
SDA214	transitional brine	1/15/2014	-23.70918	-68.25363	130.5	4418.5
SDA214		8/16/2014			47.7	1856.8
SDA234	transitional brine	8/18/2014	-23.65252	-68.24592	50.7	969.1
SDA233	transitional brine	8/18/2014	-23.66684	-68.18966	39.1	1160.2
SDA231	transitional brine	8/18/2014	-23.70074	-68.27639	81.7	1799.2
SDA198	transitional brine	1/10/2014	-23.74925	-68.28450	135.4	2078.2
SDA199	transitional brine	1/14/2014	-23.75446	-68.28071	221.7	3462.5
SDA200	transitional brine	1/14/2014	-23.78372	-68.23718	214.5	3543.9
SDA204	transitional brine	1/11/2014	-23.75003	-68.22728	212.8	4243.3
SDA205	transitional brine	1/11/2014	-23.72118	-68.22843	175.0	2828.2
SDA206	transitional brine	1/12/2014	-23.74363	-68.23806	212.1	3727.1
SDA119	nucleus brine	1/11/2012	-	-	369.5	3254.5
SDA120	nucleus brine	1/11/2012	-	-	321.5	3049.5
SDA123	nucleus brine	1/13/2012	-	-	324.7	2799.5
SDA124	nucleus brine	1/13/2012	-	-	379.6	2841.5
SDA125	nucleus brine	1/13/2012	-	-	276.8	3557.5
SDA126	nucleus brine	1/13/2012	-	-	266.5	3648.4
SDA127	nucleus brine	1/13/2012	-	-	415.0	2470.6
SDA128	nucleus brine	1/13/2012	-	-	247.5	3254.3
SDA129	nucleus brine	1/13/2012	-	-	626.5	1795.2
SDA137	nucleus brine	1/11/2012	-	-	331.3	3256.3
SDA14	nucleus brine	10/2/2011	-	-	188.6	4089.2
SDA14		1/7/2012			205.7	4113.2
SDA15	nucleus brine	10/2/2011	-	-	211.0	4103.4
SDA15		1/11/2012			237.7	3993.3
SDA16	nucleus brine	10/2/2011	-	-	248.4	4078.7
SDA16		1/11/2012			249.3	3690.1
SDA17	nucleus brine	10/2/2011	-	-	233.1	3935.9
SDA17		1/11/2012			237.7	4152.2
SDA18	nucleus brine	10/2/2011	-	-	259.4	3587.0
SDA19	nucleus brine	10/2/2011	-	-	683.9	2240.3
SDA19		1/7/2012			733.6	2054.5
SDA203	nucleus brine	1/10/2014	-	-	224.7	3259.0
SDA20	nucleus brine	10/2/2011	-	-	666.5	2050.1
SDA21	nucleus brine	10/2/2011	-	-	228.8	3596.7
SDA21		1/11/2012			247.0	3488.5
SDA22	nucleus brine	10/2/2011	-	-	278.4	3323.3
SDA22		1/11/2012			283.5	3358.5
SDA23	nucleus brine	10/2/2011	-	-	246.7	3442.8
SDA23		1/11/2012			271.4	3352.7
SDA24	nucleus brine	10/2/2011	-	-	322.1	3282.7
SDA24		1/11/2012			357.8	3205.8
SDA25	nucleus brine	10/2/2011	-	-	207.4	3926.7
SDA25		1/11/2012			232.4	3721.9
SDA26	nucleus brine	10/2/2011	-	-	212.6	4115.6
SDA26		1/11/2012			242.9	3959.6
SDA27	nucleus brine	10/2/2011	-	-	177.8	4364.2

(*continued on next page*)

Table 7 (*continued*)

Sample ID	Water type	Sample Date	latitude	longitude	Li (mmol/L)	Na (mmol/L)
SDA27		1/11/2012			173.6	4063.8
SDA28	nucleus brine	10/3/2011	-	-	242.4	3795.5
SDA28		1/6/2012			221.5	3790.7
SDA28		9/25/2012			249.6	3057.0
SDA28		1/14/2013			254.6	3791.2
SDA28		1/10/2014			232.0	3437.5
SDA28d	nucleus brine	1/7/2012			251.6	3864.1
SDA28m	nucleus brine	1/7/2012			259.8	3729.4
SDA28s	nucleus brine	1/7/2012			249.1	3521.4
SDA95	nucleus brine	1/7/2012	-	-	524.6	2560.5
SDA96	nucleus brine	1/8/2012	-	-	502.4	2583.8
SDA97	nucleus brine	1/8/2012	-	-	459.0	3290.8
SDA98	nucleus brine	1/8/2012	-	-	402.4	2988.3
SDA99	nucleus brine	1/8/2012	-	-	476.3	2836.7
SDA99		9/28/2012			365.3	2084.9

NR = not reported. Data (MPW) from Rissmann et al. (2015) included for waters in the MNT aquifer to the south. Locations of nucleus brines is proprietary information.

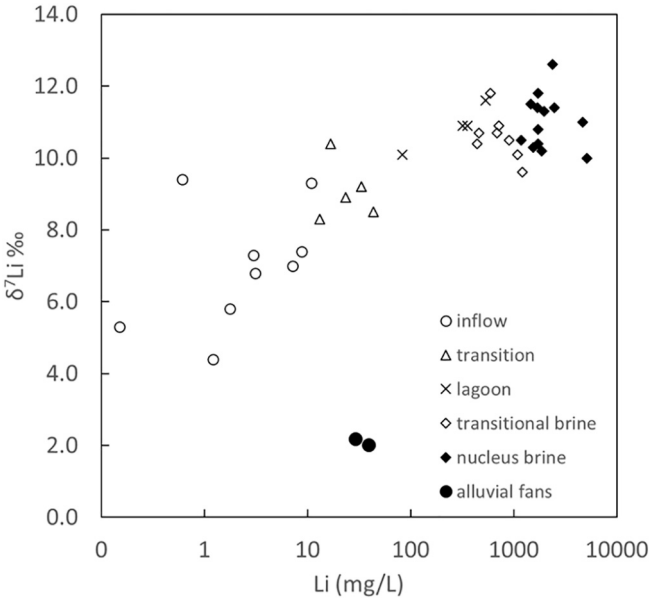

Fig. 10. Lithium concentration and δ^7Li for main water types and two alluvial fans in the Salar de Atacama basin. Leaching of alluvial fan material results in fractionation of the Li isotopes, enriching the resulting waters in ^{7}Li. Additional fractionation appears to occur in the transition zone further enriching those waters in ^{7}Li.

secondary salts have not been identified and K-bearing secondary salts such as jarosite (McCartney, 2001) and sylvite are rare. Although rigorous geochemical modeling of the observed phases and water chemistry are beyond the scope of the current study, this general trend of removal of Ca and Mg and to a lesser extent Li and K may be invoked along with the composition of inflow waters to explain the general first order observation that these solutes appear to balance in the halite nucleus and brine at different accumulation rates.

4.6. Hydrogeochemical processes contributing to lithium brine formation

Fig. 9 illustrates the geochemical evolution of inflow waters to brines in the basin in terms of the conservative elements Li and Na (Table 7). Because of the highly conservative behavior of Li (and similarly for Na) in this environment it can be used to track the evolution of the most dilute inflow waters to the highly concentrated brines. The range of Li and Na concentrations define the inflow and transition zone waters along paths of increasing concentration followed by the trend of decreasing Na with an increase in Li in the brines. Recharge (precipitation) and inflow waters (surface and shallow groundwater) become enriched in Li (and Na) through low-temperature weathering processes which likely include silicate weathering but also contributions from older salt deposits, followed by further concentration by evapotranspiration occurring down gradient and in particular where the water table intersects the surface and is expressed as shallow lagoons. The water in the lagoons evaporates and forms transitional brines which are located at shallow depths in the transition zone of the salar. These brines may mix with some of the marginal halite nucleus brines as is evident where the transitional and nucleus brines overlap in their Na and Li composition. The final process operating to form the Li-enriched brine is crystallization of halite indicated by a decrease in Na with an increase in Li and the fact that the brines are hosted in a halite aquifer.

Lithium has been used successfully used as a tracer of both low and high temperature weathering processes (e.g. Huh et al., 1998; Millot et al., 2010, Tomascak et al., 2016 and refs within) and Li isotopes have been used to understand processes across a spectrum of marine, freshwater and terrestrial environments (Burton and Vigier, 2011), oil field brines (Chan et al., 2002), continental brines (Bottomley et al., 1999 and 2003) and Li brines in salars (Munk et al., 2011; Godfrey et al., 2013). Lithium isotope fractionation is now known to be a useful tool in studies of weathering environments such as the Mono Lake basin (Tomascak et al., 2003), silicate weathering rates of volcanic rocks of different ages in Iceland based on stream water values (Vigier et al., 2009), temperature dependence of lithium isotope fractionation in clays (Vigier et al., 2006; Vigier et al., 2008), low and high temperature weathering of volcanic islands (Rad et al., 2013) and more recently for understanding potential sources of Li in the playa at Clayton Valley, NV, USA (Munk et al., 2011; Araoka et al., 2014).

In order to further investigate the hydrogeochemical processes influencing brine formation the δ^7Li and Li concentrations for the main water types in the basin and two alluvial fans (< 2 mm fraction) are compared (Fig. 10). The inflow waters range from 4.4–9.4‰ and have the lowest Li concentrations, transitional waters that undergo evapotranspiration and salt precipitation/dissolution range from about 8.3–10.4‰ with intermediate Li concentrations, lagoon waters range from 10.1–11.6‰, the transitional brines range from 9.6–11.8‰ and halite nucleus brines range from 10.2–12.6‰ at the highest Li concentrations (1000s ppm). These δ^7Li and Li concentrations are consistent with those reported in Tomascak et al. (2016) and Godfrey et al. (2013) for other Andean waters. The general pattern of increasing Li and δ^7Li from inflow waters to brines is a function of evapoconcentration which drives the Li concentration up as well as results in the formation of secondary mineral phases in the transitional salar margin

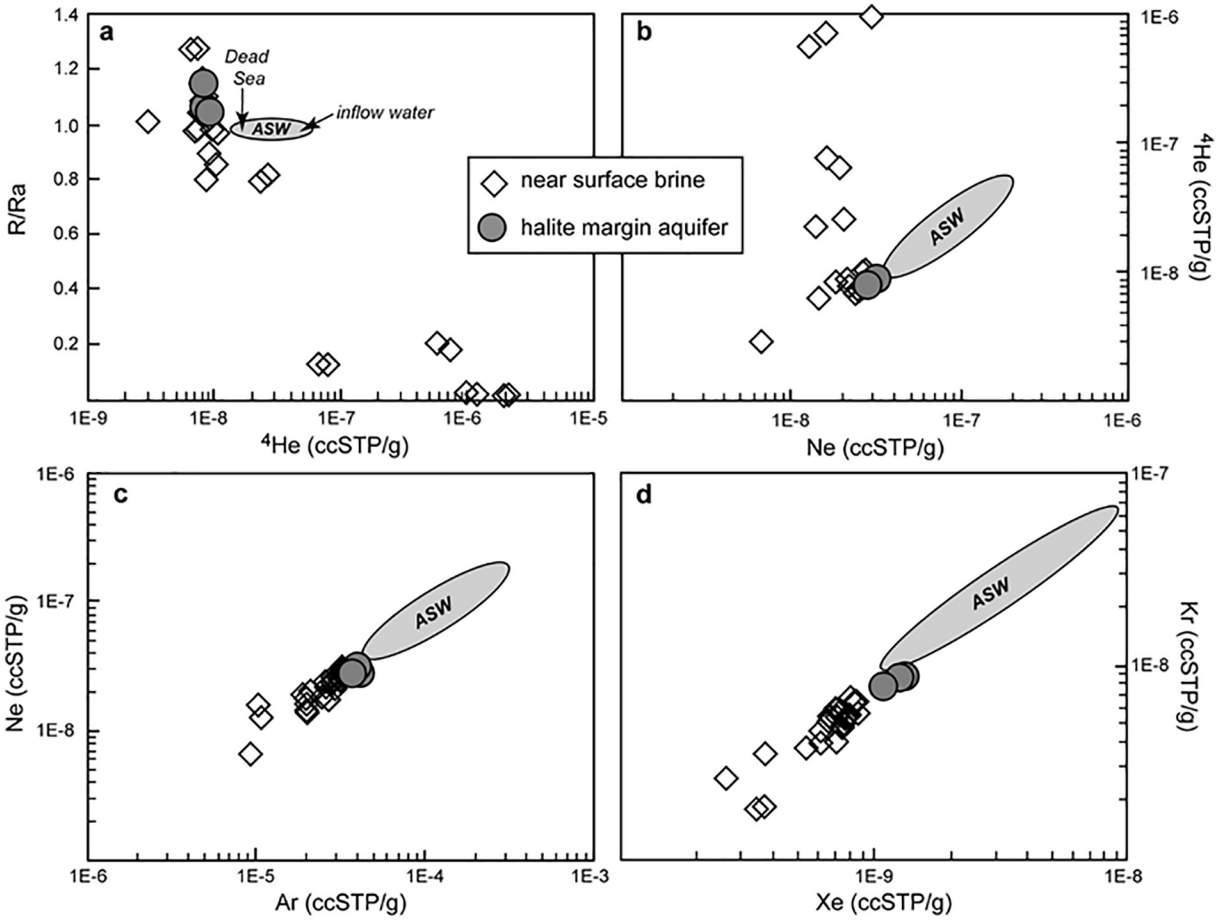

Fig. 11. Dissolved noble gas concentrations in near surface brines, compared to the range of values that would be expected in air saturated water (ASW) from SdA inflow water (5 mS/cm) and Dead Sea brines (cf. Weiss and Price, 1989) with salinities similar to SdA brines. A subset of brines from the halite margin aquifer (cf. Boutt et al., 2016) is highlighted as having a signature of recent atmospheric equilibration. The halite margin aquifer subset consists of samples SDA109, SDA111, and SDA112, locations given in Table 6.

and halite nucleus. It is evident that these secondary phases sequester ^{6}Li which results in an increase in the δ^{7}Li of fractionated water as Li concentration increases. There are also two inflow water samples that have an enriched δ^{7}Li (~9‰) which could reflect the differences in geology within the weathering watershed. Lithium is known to concentrate in the octahedral layer of clays with increasing concentrations of Li in solution, temperature, and time (Decarreau et al., 2012). The isotopes of Li fractionate during the formation of clay and other secondary minerals where ^{6}Li is preferentially incorporated into the crystal structure (e.g. Tomascak, 2004; Vigier et al., 2006; Millot et al., 2010), but there may be other secondary minerals such as salts that also sequester ^{6}Li (Godfrey et al., 2013).

Fig. 10 also shows that two alluvial fan samples (< 2 mm fractions) collected from the basin have a δ^{7}Li of about 2‰ and contain 29 and 30 ppm Li. Scant data exist on both the amounts of Li released during weathering (field and laboratory studies) as well as on the fractionation of Li isotopes during leaching of high-silica Li source rocks (Risacher and Alonso, 2001; Godfrey et al., 2013 and Jochens and Munk, 2011, see Table 4). However, what has been observed in these experimental studies is that from rocks (ignimbrite/ash and alluvial fans < 2 mm) containing on the order of < 1–20 ppm Li there is a leachable fraction of Li that is on the order of 0.01 to 1.2 mg/L (Table 4). Lithium isotope fractionation during these same leaching experiments indicates an enrichment in the resulting leachate solutions between 5.40 and 7.63‰ ^{7}Li. Therefore, the weathered alluvial fan material from the SdA basin with a δ^{7}Li of ~2‰ compared to the average inflow water of δ^{7}Li ~ 7 is a difference of 5‰ which is within the experimental results of Godfrey et al. (2013) and Jochens and Munk (2011). Subsequent enrichment of the brines in ^{7}Li can be explained by the removal of ^{6}Li during secondary salt formation. Further research on the utility of Li isotope systematics in these environments is warranted as is more work on determining the Li source rocks.

Dissolved noble gas results are presented in Table 5. Helium isotope ratios (^{3}He/^{4}He = R) ratios are reported relative to the atmosphere (Ra = 1.384E−6) such that R/Ra of air saturated water (ASW) yield a value of ~0.98 due to the slightly higher solubility of ^{4}He relative to ^{3}He (Weiss, 1970). Equilibrium concentrations of dissolved gases in hypersaline water are poorly known, but several lines of evidence lead us to interpret SdA brine signature as largely atmospheric in nature (Fig. 11). Primarily, gases of atmospheric origin have concentrations much lower than expected for fresher inflow water and similar to measurements that have been made of Dead Sea brine (also at halite saturation) (Fig. 11a). Our data also have slopes contiguous with the ASW envelope, indicating that atmospheric equilibration of the brines is the likely control on their dissolved gas concentration. Brines sampled from the halite margin aquifer, which have been shown to be in excellent communication with the modern atmosphere (cf, Boutt et al., 2016), plot closest to the Dead Sea brines. Many samples also have helium concentrations and isotope ratios similar to that expected for ASW, but two sets of samples show clear evidence for non-atmospheric sources of He (Fig. 11a–b). There are some samples that have high He concentrations and low ^{3}He/^{4}He ratios, consistent with long residence time groundwater and crustal helium production (i.e. increased ^{4}He). Others have He concentrations similar to that expected from air

saturation of brine, but have $^{3}He/^{4}He$ ratios (R/Ra = 1.0–1.27) indicative of a ^{3}He source, either magmatic (mantle derived) or cosmogenic in origin. With the exception of helium, all dissolved noble gas concentrations are indicative of brines in equilibrium with or undersaturated with respect to atmospheric composition (Fig. 11b–d).

The dominant atmospheric noble gas signature of brines in the halite nucleus confirms a near surface origin. Due to the large range of gas solubility in water as a function of salinity, it is possible to identify freshwater that has since acquired solutes but not lost its freshwater gas signal. Strong evidence for this "salting" effect is lacking in the SdA brines. However, three samples do stand out as having generally higher gas concentrations, these samples are most easily distinguished by the heavy noble gas concentrations (Fig. 11d, the halite margin aquifer). These samples are from wells and open pools along the margin of the halite nucleus where storm water pulses have been identified by water level variations and confirmed with low Li and high ^{3}H concentrations (Boutt et al., 2016).

There is minimal evidence for mantle derived ^{3}He (magmatic inputs). Although there are 11 samples with R/Ra values > 1, these might also be interpreted to result from cosmogenic production of ^{3}H (and ultimately, ^{3}He) via neutron capture by ^{6}Li. This ^{6}Li (n, α)$^{3}H \rightarrow {}^{3}He$ reaction can also result from radiogenic neutrons related to decay of U and Th and resultant α,n reactions on light elements (Andrews and Kay, 1982). In both of these cases, neutrons produce ^{3}He from the abundant isotope ^{6}Li via ^{3}H decay. As such, the intermediate product ^{3}H may also be observed in the brines. There is some evidence for ^{3}H in the uppermost nucleus brine aquifer; though this tritium, and associated chlorofluorocarbons, were presumed to result from communication between the brine and the modern atmosphere via gas exchange and precipitation (Boutt et al., 2016, Supporting Information).

Elevated He concentrations support accumulation and retention of gases within the halite nucleus brine aquifer. This is consistent with the observations of Kampf et al. (2005) that gas exchange (in the form of water vapor flux) from the halite nucleus is essentially non-existent. The fact that the samples with the highest He concentrations also have the lowest R/Ra values (cf. Fig. 10a) indicates ^{4}He production from radioactive decay in aquifer materials. Such accumulated ^{4}He is commonly used to identify old, regional groundwater (e.g., Gardner et al., 2011; Gardner and Heilweil, 2014), and ^{4}He production rates can be related to the U and Th concentrations in aquifer solids (Solomon, 2000). We know little about the U and Th content of the nucleus brine aquifer materials, mostly halite, clastics, and volcanic deposits. If we assume the U and Th contents are relatively low, the ^{4}He concentrations in some of the brines are indicative of very old water which has been confined for a long time. We will not attempt to calculate ages from the ^{4}He concentration given the very loose constraints on the system, but do suggest that they are parsimonious with other evidence and approaches that assume brine genesis on the order of Myr (Munk et al., 2016a; Corenthal et al., 2016).

General constraints on the genesis of brine in the halite nucleus can be derived from the dissolved noble gas data. It is evident that brine genesis is largely a near surface process whereby the brine is in excellent communication with the atmosphere at some point in time prior to being confined below a relatively impermeable halite crust. Following confinement, accumulation of ^{3}He and ^{4}He occurs in some areas of the brine. Together, these observations indicate a paleo near surface origin for the nucleus brine. Although mantle derived (magmatic) contributions of ^{3}He cannot be convincingly ruled out and warrant further investigation.

5. Conclusions

The results of this rigorous water and solute mass balance for the hyper-arid SdA basin indicate that the amount of water and solutes entering the basin is dependent on the sub-watershed region and that the contributing areas vary as a function of watershed characteristics. Evidence from multiple elemental and isotopic indicators support the notion that there are different sources of water with varying compositions within the SdA basin. Seasonal fluctuations in solute concentration are very small indicating that at least over the last few decades the inflow water compositions are consistent. Water stable isotopes ($\delta^{18}O$, δD) indicate consistent water sources over time but also that the isotopic composition of waters sourced from the north and northeast inflow regions to the basin are more enriched than the waters sourced from the south and southeast providing evidence of multiple sources of waters. The $^{87}Sr/^{86}Sr$ signatures of the five inflow regions provide further strong evidence of the relative source regions of solutes to the SdA basin. The water flux weighted averages predict very closely the measured average $^{87}Sr/^{86}Sr$ composition of the SdA brines, but are not a perfect match indicating that there may be some unaccounted sources of solutes and water to the brines. Not all solutes mass balance within the same timeframe further emphasizing the need to invoke sources outside the basin but also impacts from the geochemical behavior of elements derived from higher elevation sources (lakes) and along flow paths to the salar. The geochemical processes that can explain the evolution of inflow waters to brine formation in the basin include low-T weathering, evapotranspiration, formation of transition zone brines, and ultimately halite crystallization to drive Li concentration to the highest levels. Lithium isotopic composition of potential Li source rocks and waters in the basin further reveal that the processes responsible for concentrating Li to some of the highest concentrations of any known fluids on the planet include the formation of secondary mineral phases. And finally, the dissolved noble gas signatures of the brines point to a system where the brines formed in a near surface setting and have since been isolated from the atmosphere via storage in the aquifers of SdA.

Acknowledgements

The authors would like to thank Albemarle Corporation (Rockwood Litio Limitada) for the ongoing support of this research to help further the understanding of the formation of Li brines. In particular Hector Maya is thanked for his vision and backing of our work. Special thanks to Dr. Diego Fernandez and the University of Utah Strontium Isotope Geochemistry Laboratory for performing the strontium isotope analyses. Dr. Linda Godfrey is thanked for her work on measuring the lithium isotopic compositions. Dr. Birgit Hagedorn's assistance with brine sample preparation and analytical work was invaluable to the project. We also thank Matt Rogers and Annie Brownlee at the University of Alaska Anchorage Stable Isotope Laboratory for analyses of waters. Alan Rigby at the University of Utah Dissolved and Noble Gas Laboratory is thanked for assistance in the field and sample analyses. Others including UAA undergraduate and graduate students Hillary Jochens, Kayla Weller, and Haley Huff and UMASS-Amherst graduate student Lilly Corenthal for assistance with field work and sample collection. Two anonymous reviewers also helped improve the quality of this paper.

Funding

Funding for this work was primarily provided by Sociedad Litio Chileno/Rockwood Litio Limitada (now Albemarle Corporation) in the form of a research grant to the University of Alaska Anchorage and research on the sediment cores was supported by the National Science Foundation (grant number EAR1443226).

References

Alonso, H., Risacher, F., 1996. Geoquimica del Salar de Atacama, parte 1: origen de los componentes y balance salino. Andean Geol. 23 (2), 113–122. http://dx.doi.org/10.5027/andgeoV23n2-a01.

Alpers, C.N., Whitmore, D.O., 1990. Hydrogeochemistry and stable isotopes of ground and surface waters from two adjacent closed basins, Atacama Desert, northern Chile. Appl. Geochem. 5 (5–6), 719–734. http://dx.doi.org/10.1016/0883-2927(90)

90067-F.
Andrews, J.N., Kay, R.L.F., 1982. Natural production of tritium in permeable rocks. Nature 298, 361–363.
Araoka, D., Kawahata, H., Takagi, T., Watanabe, Y., Nishimura, K., Nishio, Y., 2014. Lithium and strontium isotopic systematics in playas in Nevada, USA: constraints on the origin of lithium. Mineral. Deposita 49, 371–379.
Aravena, R., 1995. Isotope hydrology and geochemistry of northern Chile groundwaters. In: Bull. Inst. Fr. Études Andines. vol. 24(February). pp. 495–503.
Aron, F., González, G., Veloso, E., Cembrano, J., 2008. Architecture and style of compressive Neogene deformation in the eastern-southeastern border of the Salar de Atacama Basin (22 30′–24 15′S): a structural setting for the active volcanic arc of the Central Andes. In: 7th International Symposium on Andean Geodynamics (ISAG 2008, Nice), pp. 52–55.
Boschetti, T., Cortecci, G., Barbieri, M., Mussi, M., 2007. New and past geochemical data on fresh to brine waters of the Salar de Atacama and Andean Altiplano, northern Chile. Geofluids 7 (1), 33–50.
Bottomley, D.J., Katz, A., Chan, L.H., Starinsky, A., Douglas, M., Clark, I.D., Raven, K.G., 1999. The origin and evolution of Canadian Shield brines: evaporation or freezing of seawater? New lithium isotope and geochemical evidence from the Slave craton. Chem. Geol. 155, 295–320.
Bottomley, D.J., Chan, L.H., Katz, A., Starinsky, A., Clark, I.D., 2003. Lithium isotope geochemistry and origin of Canadian shield brines. Ground Water 41, 847–856.
Boutt, D.F., Hynek, S.A., Munk, L.A., Corenthal, L.G., 2016. Rapid recharge of fresh water to the halite-hosted brine aquifer of Salar de Atacama, Chile. Hydrol. Process. 30 (25), 4720–4740. http://dx.doi.org/10.1002/hyp.10994.
Boutt, D.F., Corenthal, L.G., Hynek, S.A., Munk, L.A., 2018. Extreme imbalance in the modern hydrologic budget of topographic catchments along the west slope of the Andes (21–26°S). Hydrol. Process (under review).
Burton, K.W., Vigier, N., 2011. Lithium isotopes as tracers in marine and terrestrial environments. In: Baskaran, M. (Ed.), Handbook of Environmental Isotope Geochemistry. vol. 1 and 2. pp. 41–59.
Carmona, V., Pueyo, J.J., Taberner, C., Chong, G., Thirlwall, M., 2000. Solute inputs in the Salar de Atacama (N. Chile). J. Geochem. Explor., vol. 69–70, 449–452. http://dx.doi.org/10.1016/S0375-6742(00)00128-X.
Chan, L.H., Starinsky, A., Katz, A., 2002. The behavior of lithium and its isotopes in oilfield brines: evidence from the Heletz-Kokhav field, Israel. Geochim. Cosmochim. Acta 66, 615–623.
Chesson, L.A., Tipple, B.J., Mackey, G.N., Hynek, S.A., Fernandez, D.P., Ehleringer, J.R., 2012. Strontium isotopes in tap water from the coterminous USA. Ecosphere(3), 67. http://dx.doi.org/10.1890/ES12-00122.1.
Corenthal, L.G., Boutt, D.F., Hynek, S.A., Munk, L.A., 2016. Regional groundwater flow and accumulation of a massive evaporite deposit at the margin of the Chilean Altiplano. Geophys. Res. Lett. 43 (15), 8017–8025. http://dx.doi.org/10.1002/2016GL070076.
Decarreau, A., Vigier, N., Palkova, H., Petit, S., Vieillard, P., Fontaine, C., 2012. Partitioning of lithium between smectite and solution: an experimental approach. Geochim. Cosmochim. Acta 85, 314–325.
Dirección General de Aguas, 2013. Análisis de la Oferta Hídrica del Salar de Atacama, Santiago, Chile.
Eugster, H.P., 1980. Geochemistry of evaporitic lacustrine deposits. Annu. Rev. Earth Planet. Sci. 8 (1), 35–63. http://dx.doi.org/10.1146/annurev.ea.08.050180.000343.
Faure, G., 1998. Principles and Applications of Geochemistry, 2nd ed.. Prentice Hall, New Jersey, pp. 1–600.
Gardner, P.G., Heilweil, V.M., 2014. A multiple-tracer approach to understanding regional groundwater flow in the Snake Valley are of the eastern Great basin, USA. Appl. Geochem. 45, 33–49.
Gardner, P., Harrington, G.A., Solomon, D.K., Cook, P.G., 2011. Using terrigenic ^{4}He to identify and quantify regional groundwater discharge to streams. Water Resour. Res. 47, W06523.
Godfrey, L.V., Chan, L.H., Alonso, R.N., Lowenstein, T.K., McDonough, W.F., Houston, J., Li, J., Bobst, A., Jordan, T.E., 2013. The role of climate in the accumulation of lithium-rich brine in the Central Andes. Appl. Geochem. 38, 92–102.
Grosjean, M., 1994. Paleohydrology of the Laguna Lejía (north Chilean Altiplano) and climatic implications for late-glacial times. Palaeogeogr. Palaeoclimatol. Palaeoecol. 109 (1), 89–100. http://dx.doi.org/10.1016/0031-0182(94)90119-8.
Grosjean, M., Geyh, M.A., Messerli, B., Schotterer, U., 1995. Late-glacial and early Holocene lake sediments, ground-water formation and climate in the Atacama Altiplano 22–24°S. J. Paleolimnol. 14 (3), 241–252. http://dx.doi.org/10.1007/BF00682426.
Herrera, C., Custodio, E., Chong, G., Lambán, L.J., Riquelme, R., Wilke, H., Jódar, J., Urrutia, J., Urqueta, H., Sarmiento, A., et al., 2016. Groundwater flow in a closed basin with a saline shallow lake in a volcanic area: Laguna Tuyajto, northern Chilean Altiplano of the Andes. Sci. Total Environ. 541, 303–318.
Houston, J., 2007. Recharge to groundwater in the Turi Basin, northern Chile: an evaluation based on tritium and chloride mass balance techniques. J. Hydrol. 334 (3–4), 534–544. http://dx.doi.org/10.1016/j.jhydrol.2006.10.030.
Houston, J., 2009. A recharge model for high altitude, arid, Andean aquifers. Hydrol. Process. 23 (16), 2383–2393. http://dx.doi.org/10.1002/hyp.7350.
Houston, John, Butcher, A., Ehren, P., Evans, K., Godfrey, L., 2011. The evaluation of brine prospects and the requirement for modifications to filing standards. Econ. Geol. 2011, 1125–1239. http://dx.doi.org/10.2113/econgeo.106.7.1225. (Nov.).
Huh, Y., Chan, L.H., Zhang, L., Edmond, J.M., 1998. Lithium and its isotopes in major world rivers: implications for weathering and the oceanic budget. Geochim. Cosmochim. Acta 62, 2039–2051.
Ide, Y.F., Kunasz, I.A., 1989. Origin of Lithium in Salar de Atacama, Northern Chile. Geology of the Andes and Its Relation to Hydrocarbon and Mineral Resources: Houston, Texas, Circum-Pacific Council for Energy and Mineral Resources, Earth Science Series. vol. 11. pp. 165–172.
Jochens, H., Munk, L.A., 2011. Experimental weathering of lithium-bearing source rocks Clayton Valley, Nevada, USA. In: Society of Geology Applied to Ore Deposits, 2011 Meeting, Antofagasta, Chile.
Jordan, T.E., Munoz, N., Hein, M., Lowenstein, T., Godfrey, L., Yu, J., 2002a. Active faulting and folding without topographic expression in an evaporite basin, Chile. Bull. Geol. Soc. Am. 114 (11), 1406–1421. http://dx.doi.org/10.1130/0016-7606(2002)114<1406:AFAFWT>2.0.CO;2.
Jordan, T.E., Godfrey, L.V., Munoz, N., Alonso, R.N., Lowenstein, T.K., Hoke, G.D., Peranginangin, N., Isacks, B.L., Cathles, L., 2002b. Orogenic-scale ground water circulation in the Central Andes: evidence and consequences. In: 5th ISAG International Symposium on Andean Geodynamics. Institut de Recherche Pour le Développement, and Université Paul Sabatier, pp. 331–334.
Jordan, T.E., Mpodozis, C., Muñoz, N., Blanco, N., Pananont, P., Gardeweg, M., 2007. Cenozoic subsurface stratigraphy and structure of the Salar de Atacama Basin, northern Chile. J. S. Am. Earth Sci. 23 (2–3), 122–146. http://dx.doi.org/10.1016/j.jsames.2006.09.024.
Jordan, T.E., Nester, P.L., Blanco, N., Hoke, G.D., Dávila, F., Tomlinson, A.J., 2010. Uplift of the Altiplano-Puna plateau: a view from the west. Tectonics 29 (5). http://dx.doi.org/10.1029/2010TC002661.
Kampf, S.K., Tyler, S.W., Ortiz, C.A., Muñoz, J.F., Adkins, P.L., 2005. Evaporation and land surface energy budget at the Salar de Atacama, Northern Chile. J. Hydrol. 310 (1–4), 236–252. http://dx.doi.org/10.1016/j.jhydrol.2005.01.005.
Kunasz, I.A., Bell, R.R., 1979. Salar de Atacama Geochemical Exploration: Clay Exploration.
Lameli, C.H., 2011. INFORME FINAL ESTUDIO HIDROGEOLÓGICO PROYECTO “Planta de Sulfato de Cobre Pentahidratado”. pp. 0–33.
Lowenstein, T.K., Risacher, F., 2009. Closed basin brine evolution and the influence of Ca-Cl inflow waters: Death Valley and Bristol dry lake California, Qaidam Basin, China, and Salar de Atacama, Chile. Aquat. Geochem. 15 (1–2), 71–94. http://dx.doi.org/10.1007/s10498-008-9046-z.
Lowenstein, T.K., Hein, M.C., Bobst, A.L., Jordan, T.E., Ku, T.-L., Luo, S., 2003. An assessment of stratigraphic completeness in climate-sensitive closed-basin lake sediments: Salar de Atacama, Chile. J. Sediment. Res. 73 (1), 91–104. http://dx.doi.org/10.1306/061002730091.
Magaritz, M., Aravena, R., Peña, H., Suzuki, O., Grilli, A., 1990. Source of ground water in the deserts of northern Chile: evidence of deep circulation of ground water from the Andes. Groundwater 28 (4), 513–517. http://dx.doi.org/10.1111/j.1745-6584.1990.tb01706.x.
Mather, A.E., Hartley, A., 2005. Flow events on a hyper-arid alluvial fan: Quebrada Tambores, Salar de Atacama, northern Chile. Geol. Soc. Lond., Spec. Publ. 251 (1), 9–24. http://dx.doi.org/10.1144/GSL.SP.2005.251.01.02.
McCartney, J., 2001. Hydraulic and Hydrochemical Interactions in the Tilopozo Groundwater Zone, Salar de Atacama, Region II Chile. Univ. of Technol, Sydney, Sydney, Australia.
Millot, R., Vigier, N., Gaillardet, J., 2010. Behaviour of lithium and its isotopes during weathering in the Mackenzie Basin, Canada. Geochim. Cosmochim. Acta 74, 3897–3912.
Montgomery, E.L., Rosko, M.J., Castro, S.O., Keller, B.R., Bevacqua, P.S., 2003. Interbasin underflow between closed altiplano basins in Chile. Ground Water 41 (4), 523–531. http://dx.doi.org/10.1111/j.1745-6584.2003.tb02386.x.
Moraga, B.A., 1974. Estudio geologico del Salar de Atacama, Provincia de Antofagasta. vol. 29 Inst. Inv. Geol. Bol. (56 pp.).
Munk, L.A., Jennings, M., Bradley, D., Hynek, S., Godfrey, L., Jochens, H., 2011. Geochemistry of lithium-rich brines in Clayton Valley, Nevada, USA. In: 11th Biennial Meeting SGA 2011, Antofagasta, Chile, pp. 211–213.
Munk, L.A., Boutt, D.F., Corenthal, L., Huff, H.A., Hynek, S.A., 2014. Paleoenvironmental records from newly recovered sediment cores at the southeast margin of the Salar de Atacama, Chile. In: Abstract PP23C-1408 Presented at 2014 Fall Meeting, AGU, San Francisco, Calif., 15–19 Dec.
Munk, L.A., Hynek, S.A., Bradley, D., Boutt, D.F., Labay, K., Jochens, H., 2016a. Lithium brines: a global perspective. Rev. Econ. Geol. 18, 339–365.
Munk, L.A., Boutt, D.F., Hynek, S.A., 2016b. Sources of Calcium and Lithium to the Salar de Atacama, Chile, Rockwood Lithium, Internal Report.
Ortiz, C., Aravena, R., Briones, E., Suárez, F., Tore, C., Muñoz, J.F., 2014. Sources of surface water for the Soncor ecosystem, Salar de Atacama basin, northern Chile. Hydrol. Sci. J. 59 (2), 336–350. http://dx.doi.org/10.1080/02626667.2013.829231.
Pérez-Fodich, A., Reich, M., Álvarez, F., Snyder, G.T., Schoenberg, R., Vargas, G., Muramatsu, Y., Fehn, U., 2014. Climate change and tectonic uplift triggered the formation of the Atacama Desert's giant nitrate deposits. Geology 42 (3), 251–254. http://dx.doi.org/10.1130/G34969.1.
Rad, S., Rive, K., Vittecoq, B., Cerdan, O., Allegre, C.J., 2013. Chemical weathering and erosion rates in the Lesser Antilles: an overview in Guadeloupe, Martinique and Dominica. J. S. Am. Earth Sci. 45, 331–344.
Ramirez, C., Gardeweg, M., 1982. Hoja Toconao, Región de Antofagasta. Carta Geológica de Chile. Servicio Nacional de Geología y Minería de Chile. 54 (p.122).
Rettig, S.L., Jones, B.F., Risacher, F., 1980. Geochemical evolution of brines in the Salar of Uyuni, Bolivia. Chem. Geol. 30 (1–2), 57–79. http://dx.doi.org/10.1016/0009-2541(80)90116-3.
Reutter, K.J., Charrier, R., Gotze, H.J., Schurr, B., Wigger, P., Scheuber, E., ... Belmonte-Pool, A., 2006. The Salar de Atacama Basin: A Subsiding Block Within the Western Edge of the Altiplano-Puna Plateau. Active Subduction Orogeny, Andes, pp. 303–325. http://dx.doi.org/10.1007/978-3-540-48684-8_14.
Risacher, F., Alonso, H., 2001. Geochemistry of ash leachates from the 1993 Lascar eruption, northern Chile. Implication for recycling of ancient evaporites. J. Volcanol.

Geotherm. Res. 109, 319–337.
Risacher, F., Fritz, B., 1991. Geochemistry of Bolivian salars, Lipez, southern Altiplano: origin of solutes and brine evolution. Geochim. Cosmochim. Acta 55 (3), 687–705. http://dx.doi.org/10.1016/0016-7037(91)90334-2.
Risacher, F., Fritz, B., 2009. Origin of salts and brine evolution of Bolivian and Chilean salars. Aquat. Geochem. 15 (1–2), 123–157. http://dx.doi.org/10.1007/s10498-008-9056-x.
Risacher, F., Alonso, H., Salazar, C., 1999. Geoquímica de aguas en cuencas cerradas: I, II y III Regiones–Chile. 1. Ministerio de Obras Públicas, pp. 209.
Risacher, F., Alonso, H., Salazar, C., 2003. The origin of brines and salts in Chilean salars: a hydrochemical review. Earth Sci. Rev. 63 (3), 249–293. http://dx.doi.org/10.1016/S0012-8252(03)00037-0.
Rissmann, C., Leybourne, M., Benn, C., Christenson, B., 2015. The origin of solutes within the groundwaters of a high Andean aquifer. Chem. Geol. 396, 164–181. http://dx.doi.org/10.1016/j.chemgeo.2014.11.029.
Salas, J., Guimerà, J., Cornellà, O., Aravena, R., Guzmán, E., Tore, C., Von Igel, W., Moreno, R., 2010. Hidrogeología del sistema lagunar del margen este del Salar de Atacama (Chile). Bol. Geol. Min. 121 (4), 357–372.
Solomon, D.K., 2000. ^{4}He in groundwater. In: Cook, P., Herczeg, A.L. (Eds.), Environmental Tracers in Subsurface Hydrology. Kluwer Acad., Norwell, Mass, pp. 425–439.
Spiro, B., Chong, G., 1996. Origin of Sulfate in the Salar de Atacama and the Cordillera de la Sal, Initial Results of an Isotopic Study.
Strecker, M.R., Alonso, R.N., Bookhagen, B., Carrapa, B., Hilley, G.E., Sobel, E.R., Trauth, M.H., 2007. Tectonics and climate of the Southern Central Andes. Annu. Rev. Earth Planet. Sci. 35 (1), 747–787. http://dx.doi.org/10.1146/annurev.earth.35.031306.140158.
Tomascak, P.B., 2004. Developments in the understanding and applications of lithium isotopes in Earth and planetary sciences. Rev. Mineral. Geochem. 55, 153–195.
Tomascak, P.B., Hemming, N.G., Hemming, S.R., 2003. The lithium isotopic composition of waters of the Mono Basin, California. Geochim. Cosmochim. Acta 67, 601–611.
Tomascak, P.B., Magna, T., Dohmen, R., 2016. Advances in Lithium Isotope Geochemistry. Springer, Germany (195 pp.).
U.S. Geological Survey, 2018. Mineral Commodity Summaries 2018: U.S. Geological Survey. pp. 200. http://dx.doi.org/10.3133/70194932.
Vigier, N., Decarreau, A., Millot, R., Carignan, J., Petit, S., France-Lanord, C., 2006. Quantifying the isotopic fractionation of lithium during clay formation at various temperatures. Geochim. Cosmochim. Acta 70 (18, Supplement), A673. http://dx.doi.org/10.1016/j.gca.2006.06.1258.
Vigier, N., Decarreau, A., Millot, R., Carignan, J., Petit, S., France-Lanord, C., 2008. Quantifying Li isotope fractionation during smectite formation and implications for the Li cycle. Geochim. Cosmochim. Acta 72, 780–792.
Vigier, N., Gislason, S.R., Burton, K.W., Millot, R., Mokadem, F., 2009. The relationship between riverine lithium isotope composition and silicate weathering rates in Iceland. Earth Planet. Sci. Lett. 287, 434–441.
Warren, J.K., 2010. Evaporites through time: tectonic, climatic and eustatic controls in marine and nonmarine deposits. Earth-Sci. Rev. 2010, 217–268. http://dx.doi.org/10.1016/j.earscirev.2009.11.004. (Feb.).
Warren, J.K., 2016. Evaporites. In: A Geological Compedium, 2nd ed. Springer Berlin Heidelberg, pp. 1–1035. http://dx.doi.org/10.1007/978-3-319-13512-0.
Weiss, R.F., 1970. Helium isotope effect in solution in water and seawater. Science 168, 247–248.
Weiss, R.F., Price, B.A., 1989. Dead Sea gas solubilities. Earth Planet. Sci. Lett. 92, 7–10.